J. Fluid Mech. (2003), *vol.* 474, *pp.* 35–84.
DOI: 10.1017/S0022112002002446 Printed in the United Kingdom

Experimental study of the instability of unequal-strength counter-rotating vortex pairs

By J. M. ORTEGA, R. L. BRISTOL AND Ö. SAVAŞ

Department of Mechanical Engineering, University of California at Berkeley, Berkeley, CA 94720-1740, USA
e-mail: savas@me.berkeley.edu

(Received 4 May 2001 and in revised form 9 July 2002)

A rapidly growing instability is observed to develop between unequal-strength counter-rotating vortex pairs. The vortex pairs are generated in a towing tank in the wakes of wings with outboard triangular flaps. The vortices from the wing tip and the inboard tip of the flap form the counter-rotating vortex pair on each side of the wing. The flow fields are studied using flow visualization and particle image velocimetry. Both chord-based and circulation-based Reynolds numbers are of $O(10^5)$. The circulation strength ratios of the flap- to tip-vortex pairs range from -0.4 to -0.7. The initial sinuous stage of the instability of the weaker flap vortex has a wavelength of order one wing span and becomes observable in about 15 wing spans downstream of the wing. The nearly straight vortex filaments first form loops around the stronger wing-tip vortices. The loops soon detach and form rings and move in the wake under self-induction. These vortex rings can move to the other side of the wake. The subsequent development of the instability makes the nearly quasi-steady and two-dimensional wakes unsteady and three-dimensional over a distance of 50 to 100 wing spans. A rectangular wing is also used to generate the classical wake vortex pair with the circulation ratio of -1.0, which serves as a reference flow. This counter-rotating vortex pair, under similar experimental conditions, takes over 200 spans to develop visible deformations. Velocity, vorticity and enstrophy measurements in a fixed plane, in conjuction with the flow observations, are used to quantify the behaviour of the vortex pairs. The vortices in a pair initially orbit around their vorticity centroid, which takes the pair out of the path of the wing. Once the three-dimensional interactions develop, two-dimensional kinetic energy and enstrophy drop, and enstrophy dispersion radius increases sharply. This rapid transformation of the wake into a highly three-dimensional one offers a possible way of alleviating the hazard posed by the vortex wake of transport aircraft.

1. Introduction

The reviews of Rossow (1999) and Spalart (1998) highlight the technological importance and the difficulties in understanding and controlling the behaviour of the vortex wake of a subsonic aircraft, which has direct bearing on the safety and the economics of air transport. Similar issues also confront submarine designers whose purpose is to achieve stealthiness. The wake evolves into counter-rotating vortex pairs far downstream of the aircraft. The instability of this equal-strength counter-rotating vortex pair has been studied extensively during the past few decades. It has been observed (Scorer & Davenport 1970) that the vortex wake does not decay by viscous diffusion, but instead develops a sinuous instability that leads to the formation of

vortex rings. From such observations, Crow (1970) constructed his classical linear stability model, which describes the initial behaviour of an equal-strength counter-rotating vortex pair. The most unstable wavelength from these calculations compares favourably with that observed in actual trailing vortex wakes. Further research has been conducted to better understand the subsequent nonlinear behaviour of these vortex pairs. Melander & Hussain (1989), Saffman (1990), Shelley, Merion & Orszag (1993), Kida & Takaoka (1994), and others have demonstrated the processes that cause the anti-parallel vortices to reconnect and form vortex rings.

Crow's linear theory was extended to include arbitrary-strength vortex pairs. Using an asymptotic formulation that retains linear local self-induction and nonlinear potential vortex interactions, but excludes other nonlinearities, Klein, Majda & Damodaran (1995) have shown that unequal-strength counter-rotating vortex pairs are unstable regardless of the value of Γ, where Γ is the ratio of the strength of the weaker vortex to the stronger and is less than zero for counter-rotating vortex pairs. Additionally, the most unstable wavelength of the vortex pair is seen to decrease as $\Gamma \uparrow 0$. Klein *et al*. (1995) also investigated the finite-amplitude behaviour of counter-rotating vortex pairs and demonstrated that there is finite-time collapse between the vortices, that is the anti-parallel vortices make contact with one another in finite time. Their calculations showed that for unequal-strength pairs, the weaker vortex filament wraps around the stronger one, forming vortex loops. In an earlier work, Klein & Majda (1993) developed a more general asymptotic formulation that is able to explain the generation of further nonlinearities. Crow's linear stability analysis for a pair has been extended to multiple pairs, modelling the vortex wake of an aircraft with the purpose of exploring ways to hasten the destruction of the vortices (Crouch 1997; Rennich & Lele 1999; Fabre & Jacquin 2000; Fabre, Jacquin & Loof 2002).

There are only a few observations of an instability between unequal-strength counter-rotating wake vortices. One of the earlier observations of a similar type of instability is found in flow visualization photographs taken of a Boeing 747 (B-747) wake (Corsiglia & Dunham 1976). During these flight tests, smoke was injected into the counter-rotating vortex pairs that formed from the inboard flaps. After the B-747 passes overhead, a distinct sinuous instability is seen to develop along two of the vortices. The wavelength of the instability appears to be on the order of one wing span. Leonard (1974) later modelled this B-747 wake with a three-dimensional, time-dependent, inviscid calculation and obtained the results in figure 18 of Corsiglia & Dunham (1976). Through private communication with Dr Leonard, we learned that the counter-rotating inboard and outboard flap vortices have a circulation strength ratio of $\Gamma = -0.34$. It can be seen in figure 18 of Corsiglia & Dunham (1976) that the inboard flap vortex rapidly develops a sinuous instability, which has a wavelength about equal to the initial separation distance between the tip vortices. At larger downstream distances, the counter-rotating inboard and outboard flap vortices interact in such a manner that the weaker inboard flap vortex wraps around the outboard flap vortex, forming what appears to be several vortex loops.

Over the past few years, Quackenbush, Bilanin & McKillip (1996), Quackenbush *et al.* (1997, 1998) and Quackenbush, Bilanin & Carpenter (1999) have studied the interaction of unequal-strength counter-rotating vortex pairs in an effort to alleviate the sailplane wakes of military submarines. The goal of their study is to use shape memory alloys (SMA) to actively perturb the vortices and to hasten the breakup of the wake. They have modelled the flow of two counter-rotating vortex pairs with a Lagrangian-based vortex method. For the wake modelled in figure 4 of Quackenbush *et al.* (1997), $\Gamma = -0.58$ and the initial distance between the inboard and outboard

vortices is 0.275b, where b is the distance between the tip vortices. The vortex wake is perturbed at three wavelengths: 2b, 4b, and 8b. The 8b perturbation is intended to excite the Crow instability between the oppositely signed tip vortices. However, the results of Quackenbush *et al.* (1997) demonstrate that the 2b perturbation quickly becomes the most rapidly growing mode. The authors report that the time scales of the 2b mode are 3–10 times faster than that of the 8b Crow-like mode. At larger times, vortex loops form as the weaker inboard vortices wrap around the outboard vortices. Figure 4(d) of Quackenbush *et al.* (1997) shows that the loops seem to be separating from the outboard vortices and transitioning to vortex rings.

To study the stability properties of unequal-strength counter-rotating vortex pairs, flow visualization experiments were done in the wake of a wing with outboard triangular flaps (Ortega & Savaş 2001). These experiments revealed that the two counter-rotating flap/tip vortex pairs undergo a sinuous instability within 15–20 spans downstream of the wing. Qualitatively, the instability resembles the nonlinear filament analysis in Klein *et al*. (1995) and the numerical simulations in Quackenbush *et al.* (1997). Following the observations of this rapidly growing instability, we conducted further research (Bristol 2000; Ortega 2001) to quantify its behaviour and to provide an explanation for this instability mechanism. This paper presents results from this research. Following a description of the flow setup in § 2, the results of a refined flow visualization experiment are discussed in § 3. Additionally, flow visualization measurements are done in the wake of a rectangular wing to demonstrate the marked difference this instability makes in the vortex wake. Features of the instability, such as its development and nonlinear evolution, are presented. Section 4 discusses the particle image velocimetry (PIV) measurements. The data from these experiments provide a quantitative assessment of the circulation strengths of the vortices, their kinetic energy, internal structure, and trajectories up to several hundred spans downstream from the wings. In § 5, the instability wavelengths are measured from the flow visualization data and the vortex sizes, separation distances, and relative strengths from the PIV data.

One of the motivations behind this work is to explore possible ways of controlling the behaviour of the vortex wake of an aircraft. The implications of this work for controlling vortex wakes are discussed in Ortega, Bristol & Savaş (2002). Another companion paper (Bristol *et al.* 2002*a*) compares the measurements in § 5 with the most unstable wavelengths from two linear stability analyses: one that computes the stability properties of a single unequal-strength counter-rotating vortex pair and another that computes the stability properties of two unequal-strength counter-rotating vortex pairs. Additionally, CFD simulations are presented to highlight important features, such as the nonlinear dynamics and full-wake velocity and vorticity data, which could not be measured in the experiments.

2. Flow setup

A modular wing is used in this experiment to generate the wake vortices (figure 1). Depending on the type of vortex wake desired, different tabs and flaps can be attached to the trailing edge of the wing. The wing and the trailing edge tabs and flaps are made of 3.2 mm thick stainless steel sheet that is rolled to a camber radius of 17 cm. The leading edge of the wing is tapered for the first 20 mm and the trailing-edge tabs and flaps over the last 10 mm. On the underside of the wing are four 1.1 mm wide $\times$ 1.1 mm deep channels, which house dye injection tubing. For this experiment, three wing configurations are used: a rectangular-shaped wing, which has

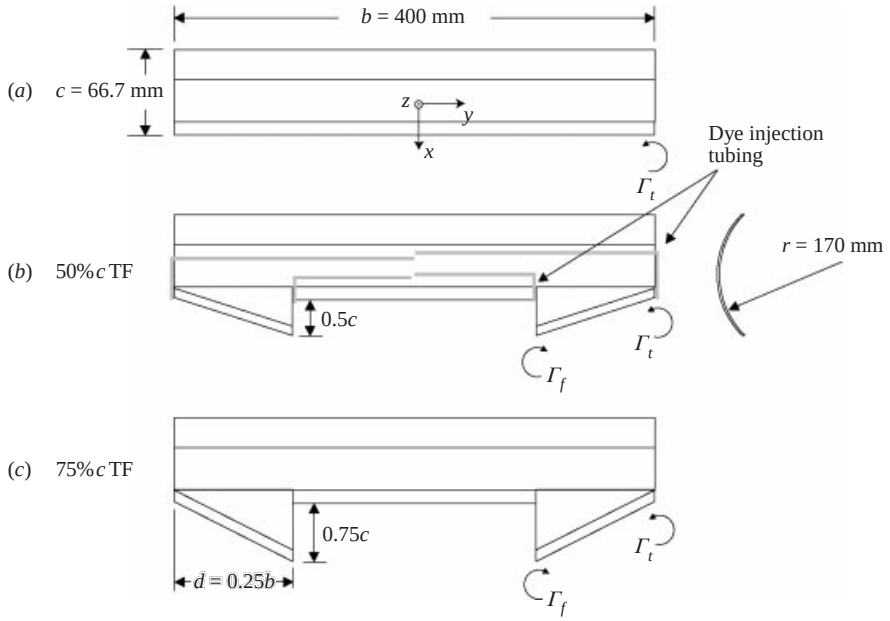

FIGURE 1. Planform and side view of the three wings used in the experiment. For the rectangular wing (*a*), only the tubes going to the wing tips are installed. The right-handed coordinate system is defined in (*a*).

a span, b, of 40.0 cm and a chord, c, of 6.67 cm (figure 1*a*); a second wing that has outboard triangular flaps, which have a span of $0.25b$ and a chord of $0.5c$ (denoted hereafter as 50%c TF, figure 1*b*); and a third wing that has outboard triangular flaps, which have a span of $0.25b$ and a chord of $0.75c$ (denoted hereafter as 75%c TF, figure 1*c*). The equal-strength counter-rotating vortex pair from the rectangular wing serves as a baseline case, against which the vortex wakes of the triangular-flapped wings are compared. In the discussions to follow, the strength of the tip vortices is Γ_t and that of the flap vortices is Γ_f. The right-handed coordinate system (x, y, z) is defined in figure 1(*a*), where the velocity vector is $\boldsymbol{u} = (u, v, w)$.

The flow visualization and PIV measurements are obtained in a towing tank, which measures 70 m × 2.4 m and has a nominal water depth of 1.5 m (Chen, Jacob & Savaş 1999). In the middle of the tank is the test section, which has glass windows that give an underwater view of the tank. A lightweight aluminium carriage is used to tow the wings down the length of the tank at high speeds. The carriage is driven by a 5-hp computer-controlled motor through a steel cable, capable of towing speeds, U_o, up to 8 m s^{-1}. Most of the experiments described here are done at $U_o = 5$ m s^{-1}, which results in a chord-based Reynolds number, $Re_c = cU_o/\nu$, of about 3.3×10^5, where $\nu = 0.01$ cm^2 s^{-1} is used for the kinematic viscosity of water. During an experiment, the carriage begins its motion at the upstream end of the tank and continues until it reaches the far end. The reason for doing this is that previous experiments have demonstrated that stopping the carriage causes the wake vortices to prematurely burst. This bursting phenomenon slowly propagates downstream along the vortices. Therefore, if the carriage is stopped too close to the test section, the data collected there soon become contaminated by this effect.

The wings are attached to the carriage by a streamlined strut, which places them approximately 0.5 m beneath the water surface. Before conducting the experiments,

Run PIV	U_o (cm s^{-1})	α (deg.)	$\frac{1}{2}(\lvert\Gamma_{or}(0)\rvert + \lvert\Gamma_{ol}(0)\rvert)$ (cm^2 s^{-1})	$\overline{\Gamma}_{ol}$ (cm^2 s^{-1})	$\overline{\Gamma}_{or}$ (cm^2 s^{-1})	Re_Γ	$\overline{KE}$ (cm^4 s^{-2})	$\bar{r}_{rmax}/b$	$\bar{r}_{lmax}/b$
10	500	3	854	−869	883	85 400	258 000	0.064	0.061
11	500	3	856	−866	868	85 600	255 000	0.064	0.061
13	500	3	821	−851	868	82 100	250 000	0.064	0.060
23	500	3	829	−896	917	82 900	267 000	0.063	0.061
15	500	0	374	−359	361	37 400	48 300	0.090	0.103
16	500	0	383	−346	365	38 300	45 400	0.090	0.100
17	500	0	381	−349	361	38 100	45 900	0.090	0.112
18	500	2	721	−727	735	72 100	189 000	0.060	0.063
19	500	2	725	−723	743	72 500	191 000	0.061	0.061
20	500	2	760	−721	733	76 000	191 000	0.058	0.060
21	300	2	388	−364	362	38 800	50 000	0.058	0.060

TABLE 1. PIV run parameters for the rectangular wing: U_o, wing speed; α, angle of attack. Measured quantities: $\frac{1}{2}(|\Gamma_{ol}(0)|+|\Gamma_{or}(0)|)$, initial total circulation; $\overline{\Gamma}_{ol}$, average left vortex circulation; $\overline{\Gamma}_{or}$, average right vortex circulation; Re_Γ, circulation-based Reynolds number of the wake; $\overline{KE}$, average kinetic energy of the wake; $\bar{r}_{rmax}/b$, average core size of the right vortex; $\bar{r}_{lmax}/b$, average core size for the left vortex.

flow visualization of the strut wake is performed using particle streaks in a CW laser light sheet to confirm that the strut is not yawed, an effect that could invalidate the subsequent measurements. Slight adjustments are made to the strut's yaw angle so that its wake is as thin as possible. In order to adjust the wing's angle of attack, α, the strut can pivot on its mounting bracket, allowing the angle of attack to vary between $\mp 12^\circ$ in 1° increments. The experiments presented here are performed at low angles of attack, $\alpha = 0, 2^\circ, 3^\circ$ for the rectangular wing and $\alpha = -1^\circ, 0, 2^\circ$ for the flapped wings (tables 1 and 2). Close observations over the wing surfaces showed that at high angles ($\alpha > 5^\circ$) of attack and lower tow speeds, the flow over the top surface shows signs of separation. Those conditions prone to flow separation are precluded, hence the low angles of attack. No direct observations are made to determine if the boundary layers on the wing remained laminar or become turbulent.

3. Flow visualization

The trailing vortices are visualized by releasing diluted fluorescent sodium salt dye (Sigma Chemical Company, No. F-6377) into the vortex cores. The container that supplies dye to the flap vortices has a dye concentration of 2 : 100 by weight and the container that supplies dye to the tip vortices has a dye concentration of 1 : 100 by weight. Both of these containers are open to the atmosphere, such that the dye is drawn into the vortices by the low pressure that exists in the vortex cores.

The test section of the towing tank is illuminated with blue light from several slide projectors (figure 2). The blue light is generated by placing a blue low-pass glass filter in the slide container of each projector. The projectors are located approximately 2 m from the viewing windows of the test section. The motion of the dye is recorded with three video cameras: two orthogonal views (y, z) and an oblique view. The overhead, orthogonal view (z) is provided by a Sony XC7500C camera with an 8 mm lens. By suspending the camera about 2 m above the water surface, the field of view at the wing depth is approximately 170 cm × 130 cm. The orthogonal, side view (y) of the

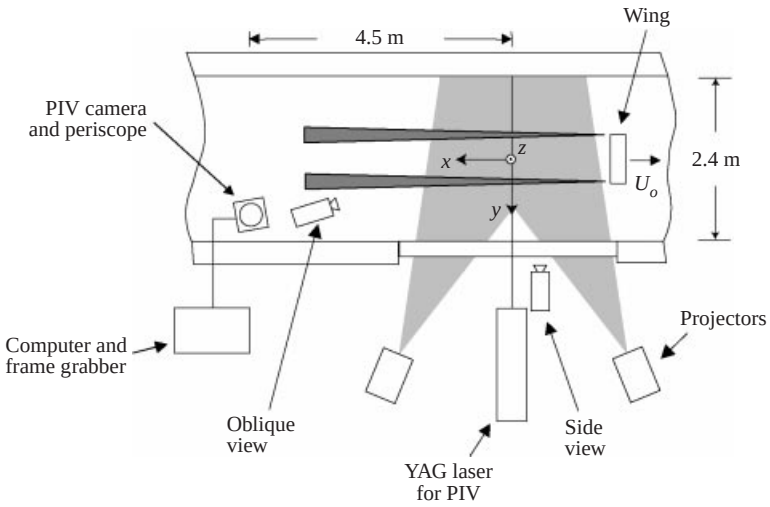

FIGURE 2. Schematic of the setup used for the PIV and flow visualization measurements. For clarity, not all of the projectors are shown.

vortex wake is recorded by placing a Texas Instruments camera (Multicam CCD) with an 8 mm lens against the glass panes in the test section. The camera is positioned at the same downstream location as the overhead Sony camera. The field of view from the Texas Instruments camera is approximately 103 cm × 77 cm at the wing centreline. Another Sony XC7500C camera gives an oblique, downstream view of the test section. This camera is housed in a waterproof cylindrical shell and is suspended in the test section such that its 8 mm lens penetrates the water surface to a depth of about 10 cm. The two orthogonal cameras are calibrated by recording a ruler at several depths and lateral locations in the test section. This information is later used to extract the instability wavelengths and other flow features that are recorded in the dye visualization images. A total of 24 flow visualization runs are made by varying the wing towing speed, angle of attack, and type of wing. The runs are spaced by approximately 20 minutes, allowing the water in the tank to become quiescent for the next run.

Since the wakes of the triangular-flapped wings are highly three-dimensional, volumetric flow visualization is a vital element in understanding the vortex dynamics in the trailing wakes. The observations made with this technique provide much more insight into the flow physics than the two-dimensional PIV measurements. Furthermore, without the flow visualization data, the PIV data would have been difficult, if not impossible, to interpret correctly at times. In the following discussions, the fluorescent dye is taken to be a marker of the vorticity in the flap and tip vortices. However, the dye does not mark all of the vorticity in the wake. The reason for this is that the dye is released at only four distinct points and not along the entire vortex sheet generated by the wings. Since the molecular diffusivity of water is much smaller than its momentum diffusivity, the dye remains as a partial marker of the vortex sheet, which rapidly rolls up into vortices. Hence, in the rolled-up wake, *the dye marks vorticity, but not all vorticity is marked by dye*. At larger downstream distances, only vortex structures that correlate well with themselves both spatially and temporally are identified and discussed. Therefore, if a large dispersal of dye is observed in the wake, no attempt is made to relate this to a large dispersal of vorticity. The PIV measurements will later be employed to quantify the spread of vorticity in the flows.

3.1. *Rectangular wing*

The flow visualization data of the rectangular wing's wake ($U_o = 500\,\mathrm{cm\,s^{-1}}$, $\alpha = 3^\circ$) are shown in figure 3. At $x/b = 0$, the wing is in the centre of the test section. The downstream distance, x, is found by the transformation $x = U_o t$, where t is the time since the wing passed through the light sheet. The black, nearly vertical lines in these top-view images are shadows cast by two of the steel beams that support the test section window. After the two counter-rotating tip vortices form, they descend rather gently in the test section. While not exactly parallel, the vortices display only a minimal amount of distortion, which is evident in the slight undulations visible in the side-view images (not shown here). Additionally, 'bulges' in the vortex core sizes are observed to travel downstream (to the left) along the length of the vortices at a speed of order $0.5\,\mathrm{m\,s^{-1}}$. The velocity of these bulges is not constant in time, but varies periodically as they make their way through the test section. The still top-view images do not clearly demonstrate these observations of the bugles. It is not until the vortices approach the bottom of the tank that they begin to exhibit some signs of the long-wavelength Crow instability ($x/b = 144$ and 186). At later times, the vortices interact strongly with the bottom of the tank and break apart.

3.2. *Triangular-flapped wings*

Unlike the wake of the rectangular wing, the wake of the triangular-flapped wings becomes highly three-dimensional as a sinuous instability rapidly develops between the unequal-strength counter-rotating flap and tip vortices. This instability is consistently observed for all towing speeds and angles of attack. The results from the flow visualization experiments for the two triangular-flapped wings (figures 1*b* and 1*c*) are shown in figures 4–6 and figures 8–10, respectively.

3.2.1. *Observations for the* 50%c *TF wing: Run FV* 1, $\alpha = 2^\circ$, $U_o = 500\,\mathrm{cm\,s^{-1}}$

Figures 4–6 show the flow visualization (FV) images of the downstream, side, and top views, respectively, at several downstream locations for the 50%c TF wing (figure 1*b*). For this particular run, the angle of attack is 2° and the towing speed is $500\,\mathrm{cm\,s^{-1}}$. The large bright spot in the side view images (figure 5) is due to the reflection of one of the projectors. The wing and four dye trails are visible in the three views at $x/b = 0$. After their initial formation, the flap and tip vortex pairs orbit outwardly on either side of the wing about their common vorticity centroids. PIV measurements in the wake of this wing at the same conditions reveal that $\Gamma_f/\Gamma_t = -0.37$. At approximately 15 spans downstream or $3\pi/4$ radians through the orbit period, instability waves are observed to rapidly develop on the weaker flap vortices. The wavelength of the instability is on the order of one wing span or four times the separation distance between the flap and tip vortices. This wavelength is shorter than that of the Crow instability between equal-strength counter-rotating vortices. The instability waves on the left and right flap vortices grow independently of one another. From the top-view images in figure 6, the distortion due to the surface waves is visible at $x/b = 18$ and 21. The disturbance amplitudes quickly grow such that the flap and tip vortices on the left-hand side make contact at about 20 spans and those on the right-hand side at 25 spans. During the growth of the instability, the perturbations on the flap vortices remain at a relatively fixed orientation with respect to the rotating reference frame of the flap and tip vortices. Consequently, the use of the unit x/b is not quite exact, since it emphasizes the fact that the vortices were generated at one point in time. Perhaps a better characteristic time is the orbital period of the vortex pairs or the descent time of the vortex system. For the remainder

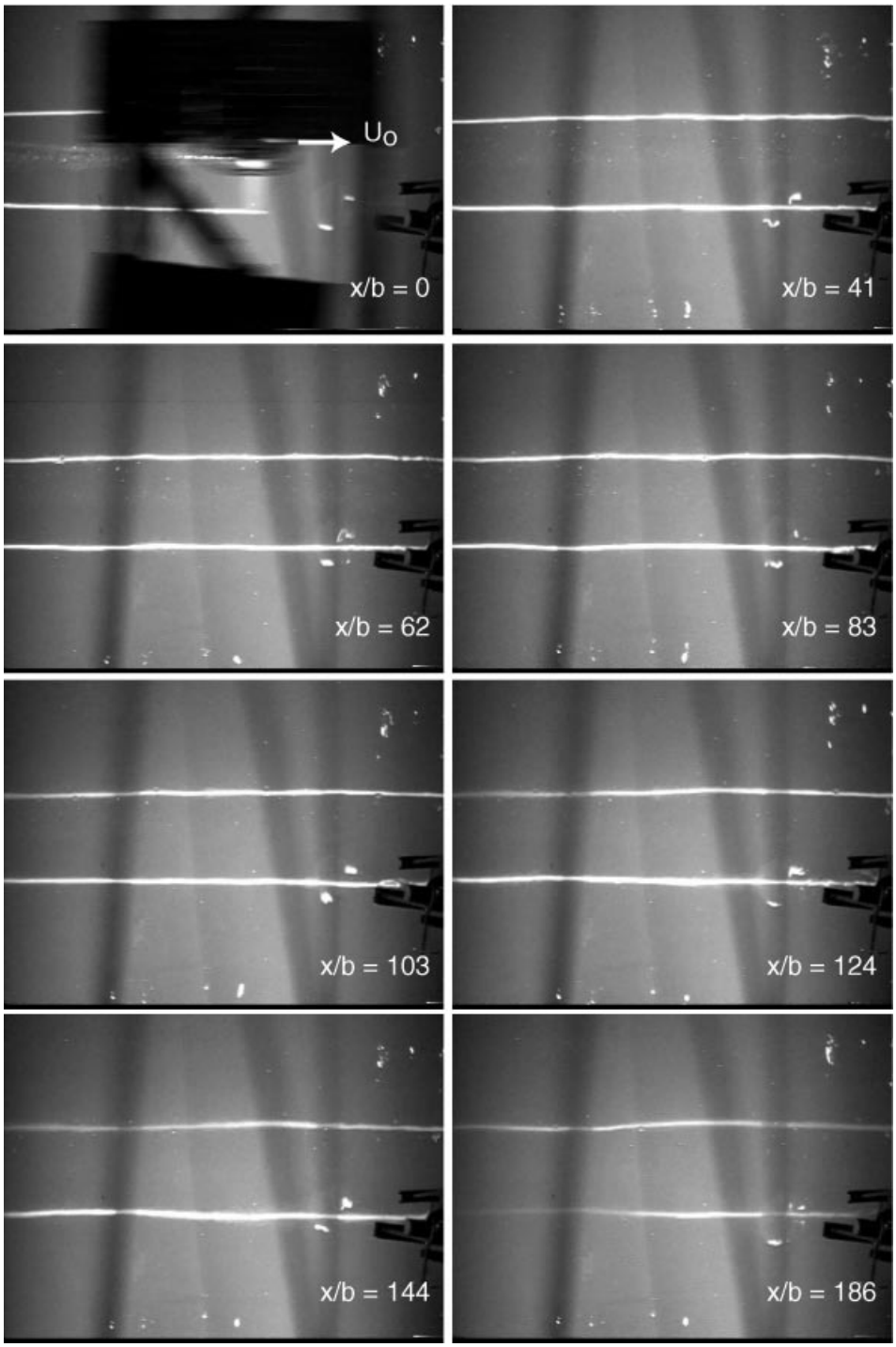

FIGURE 3. Top view of the rectangular wing's wake (Run FV 16, $U_o = 500\,\mathrm{cm\,s^{-1}}$, $\alpha = 3.0^\circ$). Note that the frames are not evenly spaced in x/b.

of this paper, the unit x/b will be used in describing the experimental observations. However, in Bristol *et al*. (2002*a*), which describes the linear stability characteristics and CFD simulations of two- and four-vortex systems, the orbital period of the vortex pairs will be employed as the characteristic time scale.

As the instability progresses, the flap vortices wrap around the tip vortices, forming Ω-shaped loops that have a structure similar to figures 13 and 16 in Klein *et al*. (1995). The spiral 'feet' of these loops behave like vortex helices around the tip vortices and advect inward toward each other. This extends the loops in the vertical direction, as is evident in the side-view images. By 45 spans, the loops are oriented vertically and are flung across the centre of the wake. As the loops approach the wing centreline, they pinch off into vortex rings, occasionally colliding with rings from the opposite side of the wing. The vortex rings that reach the opposite side of the wake collide with the remnants of the tip vortices. As the rings approach the tip vortices, their diameters increase roughly by a factor of two, resulting in an 'm'-like structure in the wake, which is visible in the top view at $x/b = 103$. By 175 spans, the dye is completely dispersed in the test section and no coherent dye patterns are visible in the wake. The downstream view and side view do, however, indicate the presence of downwash at this downstream location.

The spiral 'feet' of the 'Ω'-loops at about $x/b = 30$ in figures 4–6 show intense dye patterns which are reminiscent of bursting. The resolution of neither the flow visualizations nor the velocity measurements presented later are sufficient to make definitive statements about the nature of these features. Based on the observations of the dye filaments, however, a qualitative description may be presented. As the flap vortex wraps around the tip vortex, forming the Ω-loops, the spiral feet of an Ω-loop may be thought of as two *vortex bushings* which are moving toward each other. Their induced flow fields are also moving parcels of fluid towards each other, at even higher velocities. It is likely that the collision of these oppositely moving masses of fluids is causing the bursting at the feet of the Ω-loops immediately before the vortex reconnection that results in detached vortex rings. The internal dynamics of a vortex bushing will add further complexity to this event. For example, the bushings will tend to form toroidal spiral vortex sheets that will further spread the dye radially. The axial flow induced by these bushings around the core of the stronger tip vortex, however, is not immediately obvious.

To illustrate the vortex-connection and re-connection processes that are occurring in the wake described above, a useful exercise is to make a filament cartoon of the vortices and trace through the vortex interactions (figure 7). Let the flap and tip vortices have strengths of $-\Gamma_a$ and $\Gamma_a + \Gamma_a + \Gamma_b$, respectively. As will become evident shortly, these circulation strengths are chosen to make the following analysis more tractable and are useful when $\Gamma_f/\Gamma_t > -0.5$. Initially, the flap and tip vortices are parallel as shown figure 7(*a*). As the vortices orbit about one another, the flap filaments develop finite-amplitude perturbations (figure 7*b*), resulting in the contact of the flap and tip vortices (figure 7*c*). Neglecting the details of the vortex connection process, the flap filaments join with the Γ_a filament of the tip vortex, forming vortex rings (figure 7*d*). Assuming that there are no collisions in the centre of the wake (the vortex rings are staggered for the purpose of this illustration), the vortex rings travel to the opposite side of the wake (figure 7*e*) and there interact with the tip vortices. To keep the circulation constant along the length of the filaments, the upper halves of the vortex rings connect with the remaining Γ_a filament of the tip vortex, yielding the 'm'-like structure observed in the flow visualization images (figure 7*f*). Meanwhile, the remaining halves of the vortex rings form secondary vortex loops

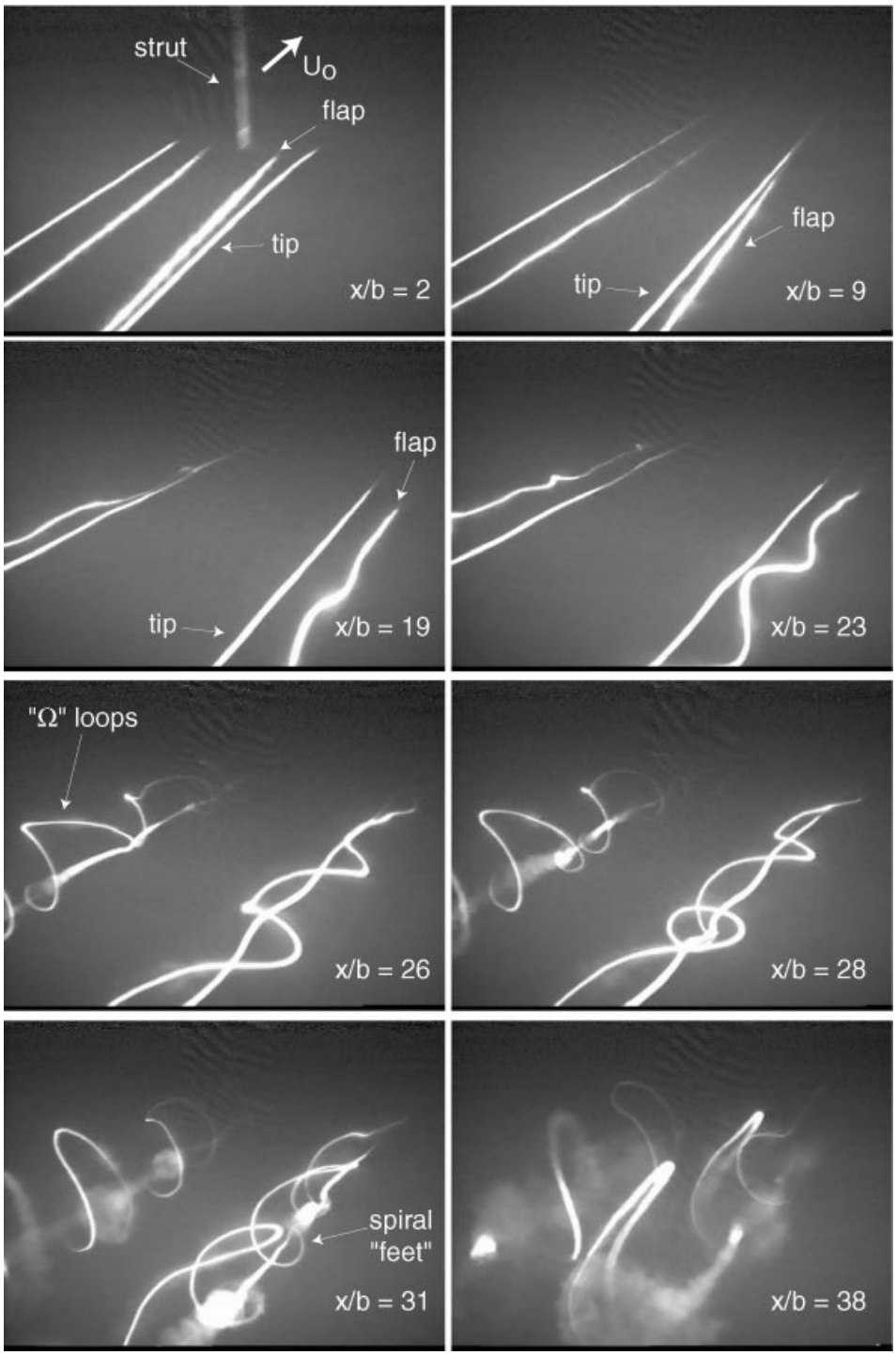

FIGURE 4. Downstream view of the triangular-flapped wing (Run FV 1, 50%c TF, $U_o = 500\,\mathrm{cm\,s^{-1}}$, $\alpha = 2.0°$). Note that the frames are not evenly spaced in x/b.

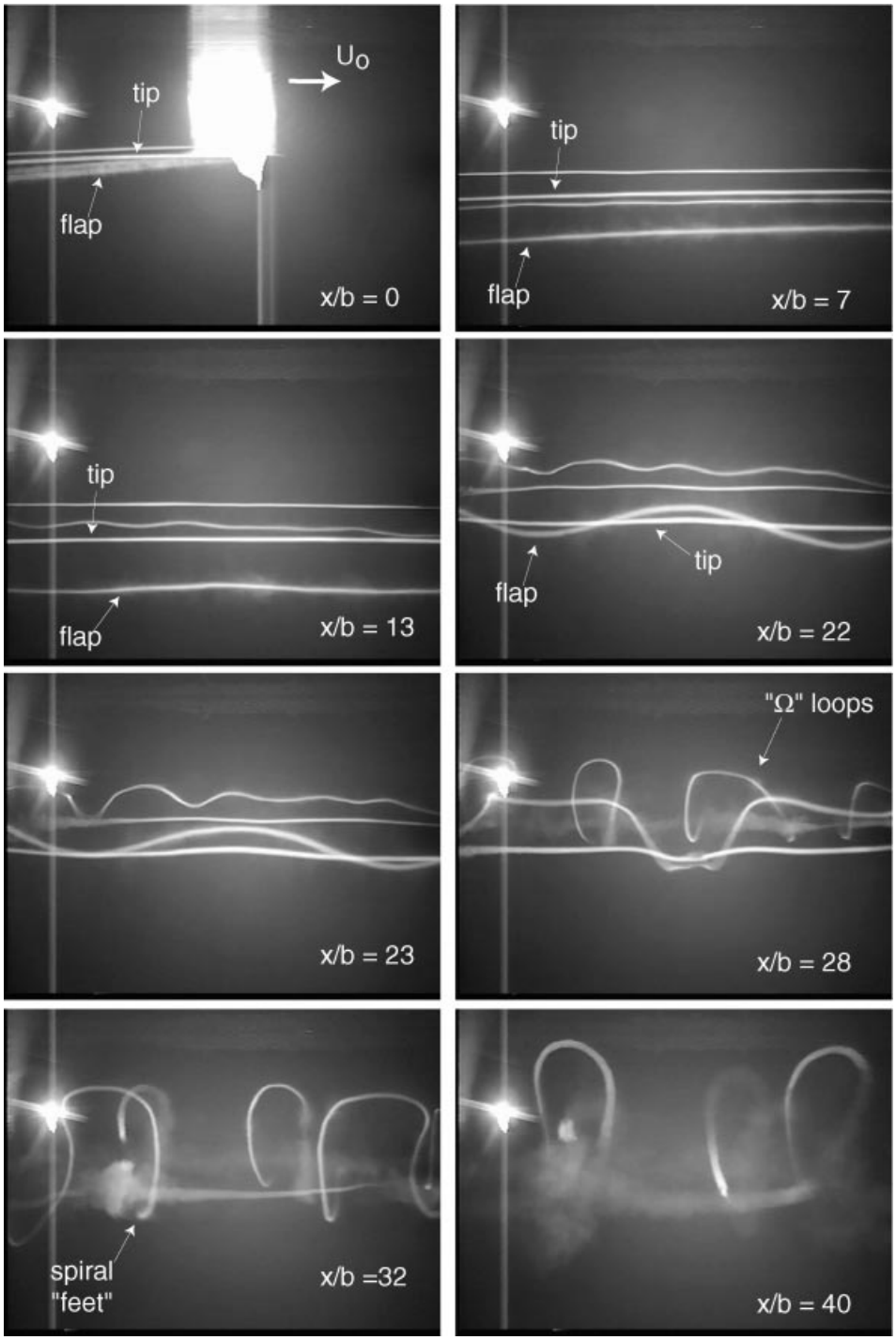

FIGURE 5. Side view of the triangular-flapped wing (Run FV 1, 50%c TF, $U_o = 500\,\mathrm{cm\,s^{-1}}$, $\alpha = 2.0°$). Note that the frames are not evenly spaced in x/b.

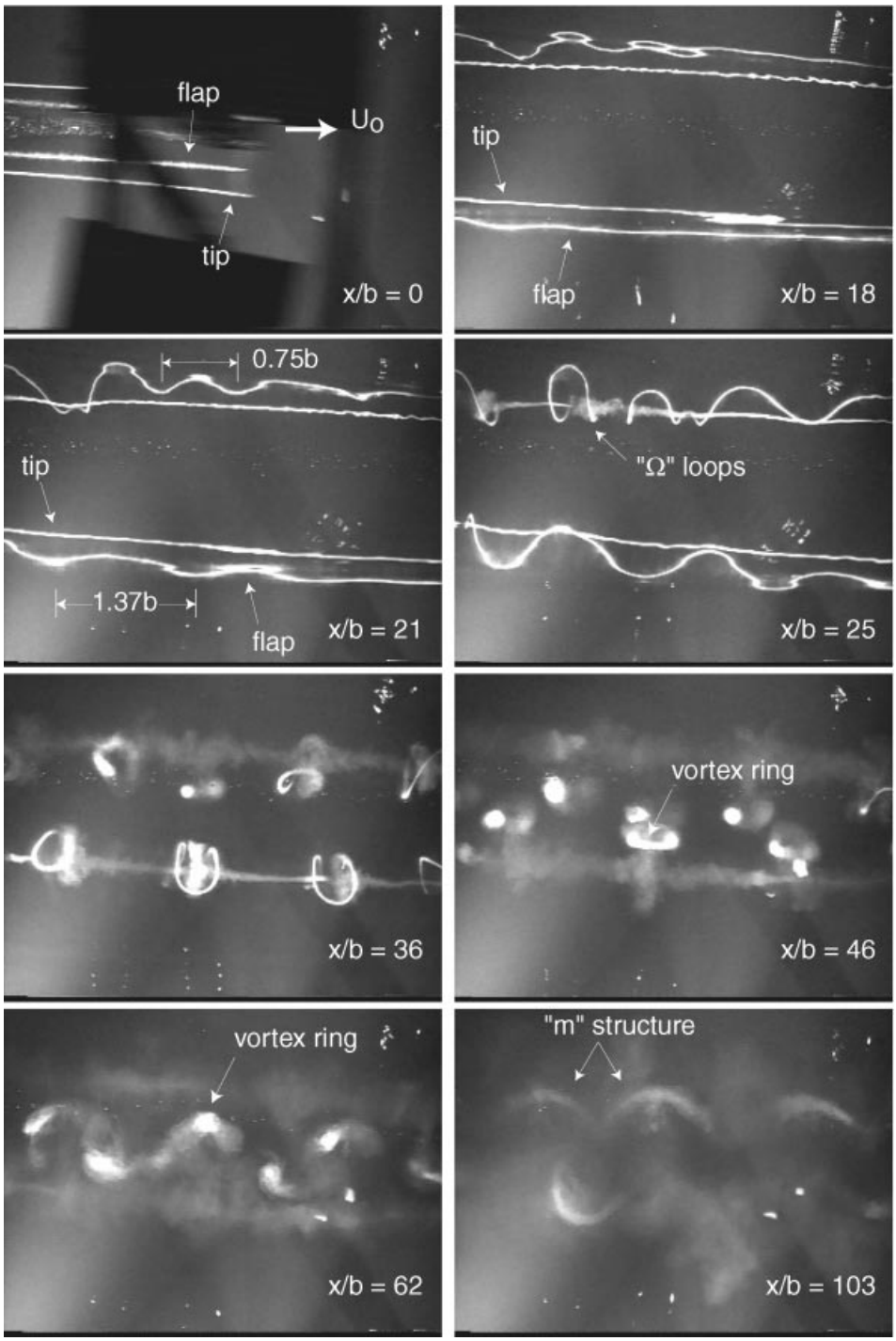

FIGURE 6. Top view of the triangular-flapped wing (Run FV 1, 50%c TF, $U_o = 500\,\mathrm{cm\,s^{-1}}$, $\alpha = 2.0°$). Note that the frames are not evenly spaced in x/b.

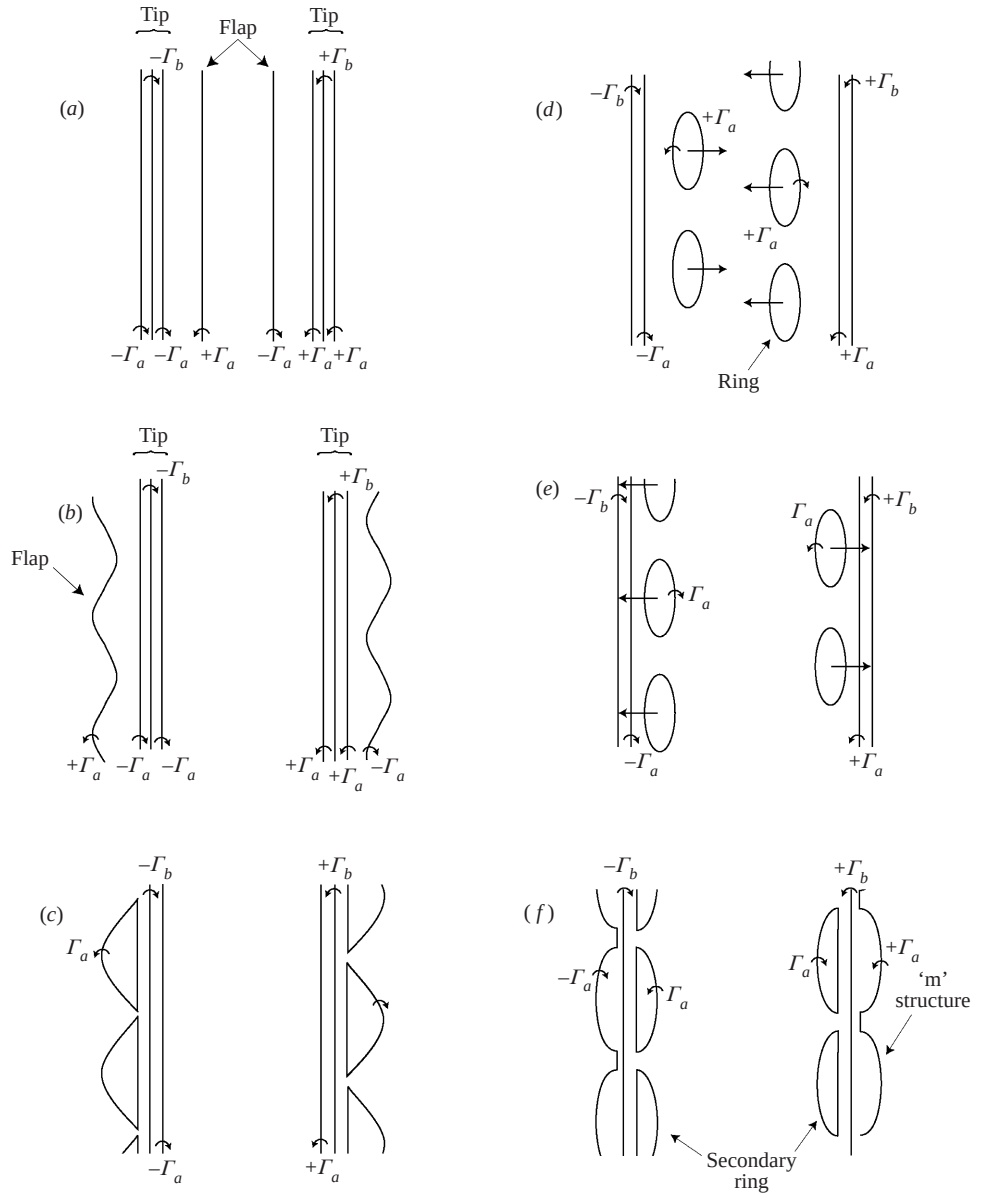

FIGURE 7. A filament model of the evolution of the vortex interactions that are observed in the wake of the 50%c TF wing at $\alpha = 2.0°$.

with the Γ_a portion of the tip filament. Due to the large dispersal of dye, it is difficult to clearly observe the existence of secondary loops in the flow visualization images.

3.2.2. *Observations for the* 50%c *TF wing: Run FV* 3, $\alpha = -1°$, $U_o = 500\,\mathrm{cm\,s^{-1}}$

The flow visualization pictures for this run are shown in figures 8–10. By decreasing the angle of attack to $-1°$, the vortex wake exhibits a somewhat different behaviour than that in Run FV 1. The reason for this is that the flap vortex is stronger than the tip vortex. PIV measurements show that $\Gamma_f/\Gamma_t = -0.55$ at these conditions.

Additionally, this angle of attack causes the overall vortex strengths to be weaker so that the pressure in the vortex cores is higher than that of the 2° runs. Consequently, the vortices draw less dye into their cores, causing the dye trails in figures 8–10 to appear fainter than those for Run FV 1. By approximately 20 spans or $\pi/2$ radians through the orbit period, a long-wavelength instability, which is slightly larger than that in Run FV 1, appears on the flap vortices. As this instability grows, the tip vortices also exhibit perturbations of the same wavelength, though their amplitude is smaller than the disturbances on the flap vortices (top view, $x/b = 23$–35). From the side-view images at 19–26 spans, a higher-wavenumber instability can be seen on the flap vortices. The wavelength of this instability is on the order of the flap/tip separation distance. This instability is repeatedly observed in the −1° runs for triangular-flapped wings at both $U_o = 300$ and $500\,\mathrm{cm\,s^{-1}}$. The source of this instability is uncertain, but, given its short wavelength, it could be caused by an 'elliptic' mode (Widnall, Bliss & Tsai 1974; Leweke & Williamson 1998; Bristol 2000; Bristol, Ortega & Savaş 2002*b*). However, this instability does not appear to have a significant impact on the vortex wake. By 31 spans or $3\pi/4$ radians through the orbit period, the left-hand side flap and tip vortices make contact with one another. After a few more spans, the right-hand side pair does the same. As the vortices in either of the pairs make contact, the stronger tip vortices 'reach out' to the flap vortices (side view, $x/b = 35$). The resulting structure of the flap and tip vortices bears a resemblance to figure 13 of Klein *et al*. (1995), which is based on a nonlinear filament calculation for a single vortex pair with $\Gamma = -0.5$.

The Ω-loops that develop from the flap vortices are slightly larger than those of Run FV 1 due to the longer wavelength of the instability (top view, $x/b = 39$). As the loops' 'feet' spiral around the tip vortices, they advect inward towards one another, which, in turn, extends the loops vertically. While the flap vortices wrap around the tip vortices, the tip vortices exhibit a helical structure as indicated in figure 10 at $x/b = 50$. Eventually, the loops pinch off into vortex rings, which travel upwards to the water surface. Unlike the 2° case, there is little exchange of dye across the wing centreline. By 125 spans, there are no coherent dye features visible in the wake. Additionally, the side and downstream views show that there is no evident downwash in the test section. This is not to say that the wake has been completely dispersed, since it is probable that the dye is too dispersed to indicate any salient features in the wake. The PIV measurements presented below provide a quantitative analysis of the behaviour of the wake at these large downstream distances.

The qualitative behaviour of the instability does not appear to depend strongly on the size of the triangular flaps. Consequently, the flow visualization runs done with the 75%c TF wing are similar to those of the 50%c TF wing. For all of the flow visualizations runs with the triangular-flapped wings, the instability initially occurs on the weaker flap vortices and has a wavelength that is on the order of one wing span. The perturbation amplitudes on the flap vortices grow rapidly, such that the flap and tip vortices eventually make contact with one another. This observation is consistent with the conclusions of Klein *et al*. (1995), which demonstrated that counter-rotating vortex pairs exhibit a finite-time collapse.

The flow visualization data provide an excellent qualitative description of the instability that arises between the unequal-strength counter-rotating vortex pairs. With these data, the highly complex, three-dimensional vortex interactions are easily identified as the instability becomes nonlinear. The one drawback of the flow visualization is that it does not lend itself to other quantitative measurements, such as the circulation strengths of the vortices, their kinetic energy, and internal structure. When

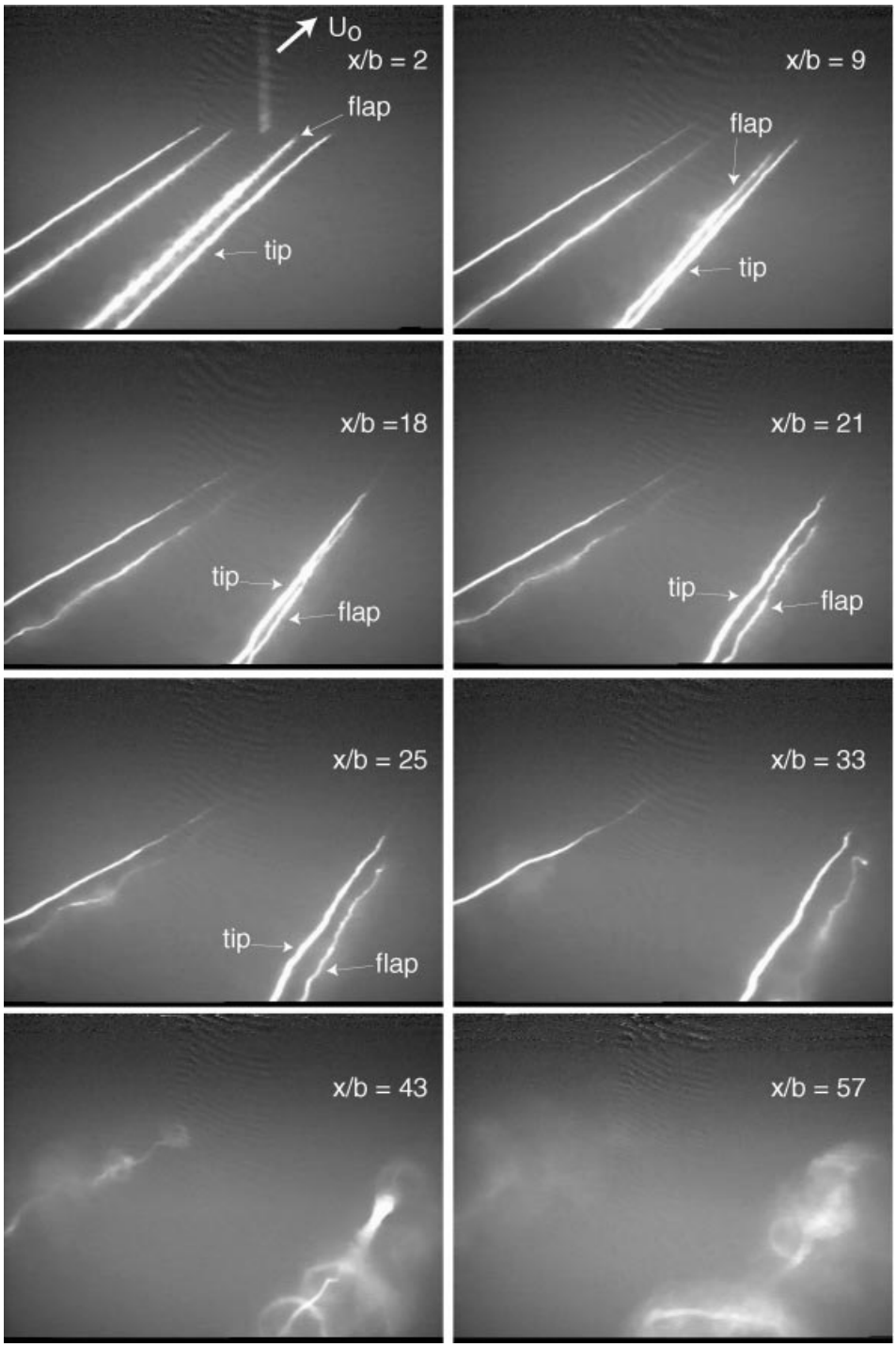

FIGURE 8. Downstream view of the triangular-flapped wing (Run FV 3, 50%c TF, $U_o = 500\,\mathrm{cm\,s^{-1}}$, $\alpha = -1.0°$). Note that the frames are not evenly spaced in x/b.

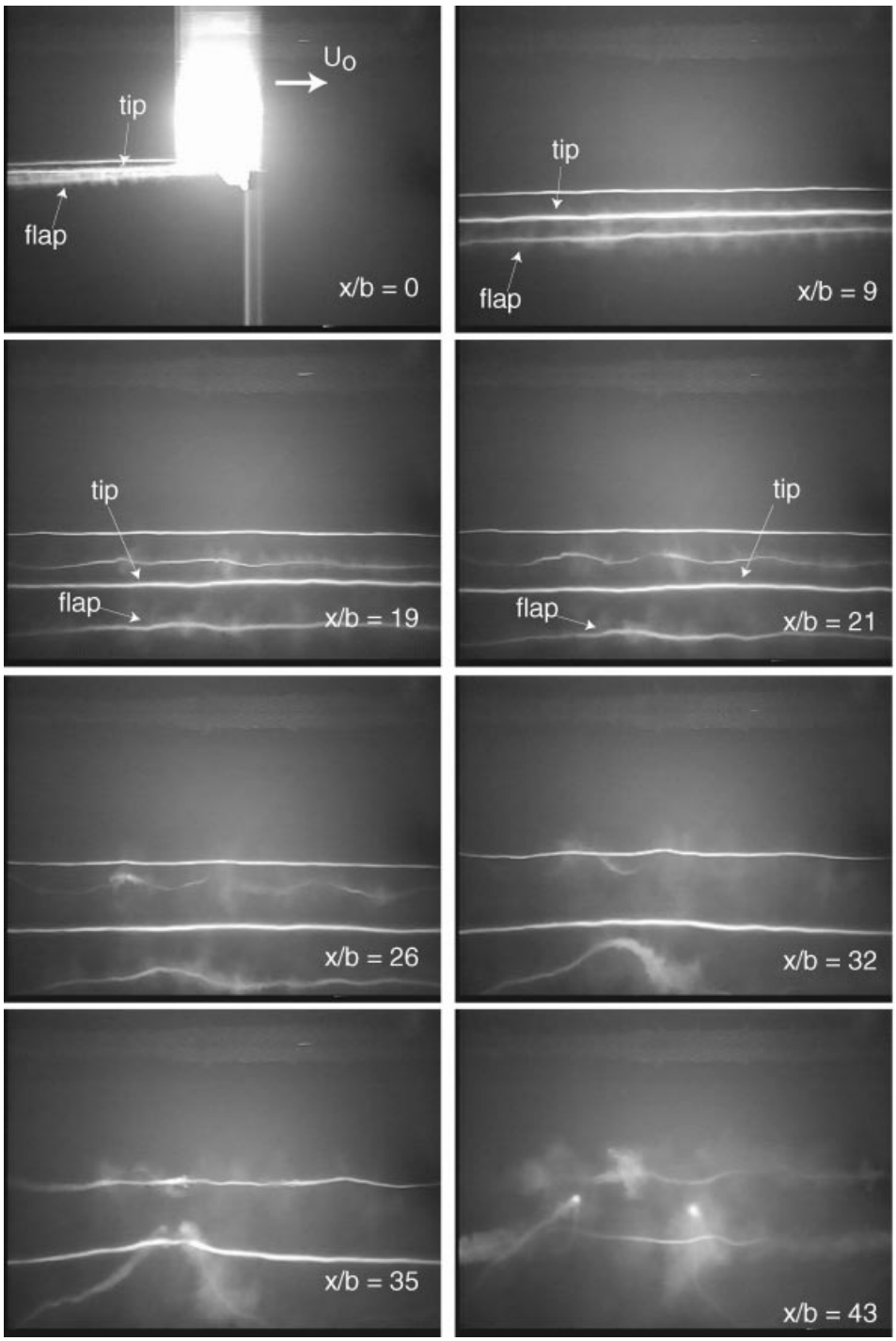

FIGURE 9. Side view of the triangular-flapped wing (Run FV 3, 50%c TF, $U_o = 500\,\mathrm{cm\,s^{-1}}$, $\alpha = -1.0°$). Note that the frames are not evenly spaced in x/b.

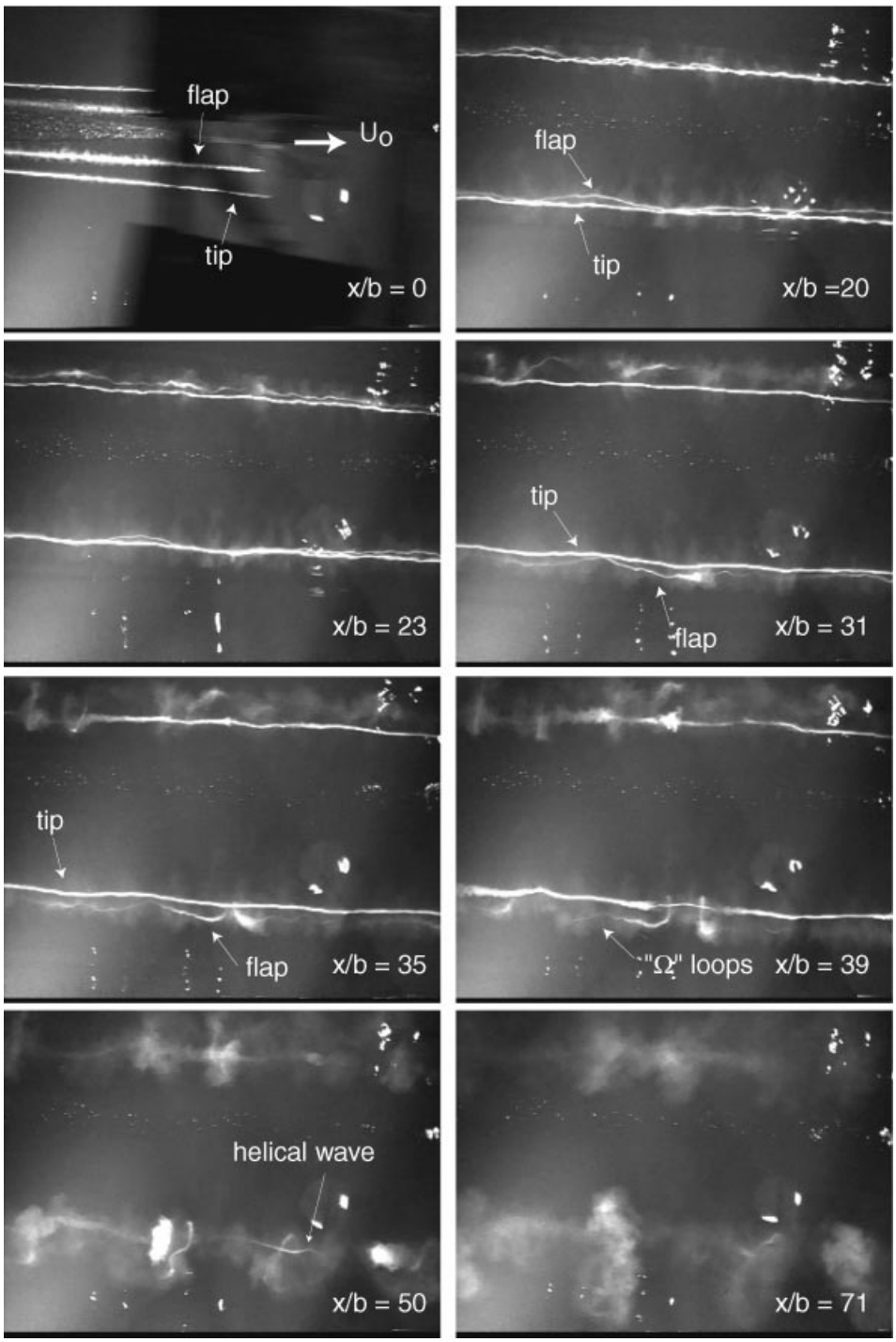

FIGURE 10. Top view of the triangular-flapped wing (Run FV 3, 50%c TF, $U_o = 500\,\mathrm{cm\,s^{-1}}$, $\alpha = -1.0°$). Note that the frames are not evenly spaced in x/b.

the dye becomes dispersed, it is also difficult to determine what is occurring in the vortex wake. For these reasons, the two-dimensional PIV measurements discussed in the following section are carried out to quantify the behaviour of the vortex wake at large downstream distances.

4. PIV measurements

Velocity and velocity-gradient measurements of the vortex wakes are made with a particle imaging velocimetry (PIV) system, a schematic of which is shown in figure 2. A Kodak Megaplus ES 1.0 (1008 pixels $\times$ 1018 pixels) digital camera is placed 4.5 m upstream of a 1 cm thick light sheet generated by a dual-head pulsed YAG laser (New Wave Gemini). To produce the light sheet, the laser beams are passed through a cylindrical lens. With a 50 mm lens attached to this camera, the field of view at the light sheet is approximately 60 cm $\times$ 60 cm. The camera acquires image pairs at 15 Hz, where the images within each pair are separated by from 6 ms to 12 ms, depending on the wing towing speed. Because the wakes of the triangular-flapped wings spread out so much, only the right half of the triangular-flapped wing is imaged. The towing tank test section was seeded with 40 micron silver-coated spheres (Potters Industries) that have a specific gravity of 0.9. The PIV camera views the particles through a periscope that places the camera approximately 120 cm beneath the water surface. To minimize its influence on the wake vortices, the periscope is suspended only 15 cm away from the tank's sidewall, causing a 16° skew in the images. The images from the camera are transferred to a computer via a digital frame grabber (Matrox Genesis-LC).

A total of 11 runs with the rectangular wing and 24 runs with the triangular-flapped wings are made. The time between sequential runs is approximately twenty minutes. Because the particles tend to become dispersed after several runs, the test section of the tank is seeded every three to four hours during the data acquisition process. Additionally, several PIV images are recorded of the background flow in the test section prior to each run. With these images, the background velocity fluctuations are determined to be of order 1 cm s^{-1} and have length scales of order 20 cm.

4.1. *Data processing*

The PIV images are first digitally corrected to remove the skew that results from the lateral offset of the camera/periscope assembly. Because of this correction process, the resulting images have a size of 1086 pixels $\times$ 1018 pixels. Another consequence of the camera's distance from the light sheet is that the particle images, which are exposed for only 6 ns, appear to be very dim. To improve their quality, the images are digitally enhanced (Ortega 2001).

The PIV processing is done with an adaptive Lagrangian parcel tracking (aLPT) (Sholl & Savaş 1998; Tsuei & Savaş 2001) algorithm. This algorithm utilizes interrogation windows that are advected and deformed according to the local velocity and velocity-gradient fields, improving the quality of the data in regions of strong deformation. The outputs of aLPT are the two-dimensional velocity vector field, u_i, and its gradient tensor, $\partial u_i/\partial x_j$, which is computed spectrally. The axial vorticity, ω, is determined from the velocity-gradient tensor. For this experiment, processing of the 1086 pixel $\times$ 1018 pixel images results in data fields that are 66 step $\times$ 62 step, giving a resolution of about 1 cm/step with a 50% overlap between successive steps. The time separation between the data fields is 66 ms (15 Hz) such that time scales of the flow shorter than 133 ms are not accessible.

To provide some measure of the accuracy of aLPT, synthetically generated PIV image pairs of single Lamb–Oseen vortices are processed. For this purpose, four vortex sizes and two vortex strengths are chosen, which are comparable to the those studied experimentally. The normalized standard deviations between the analytical input and the processed output velocity and vorticity fields are calculated for each synthetic PIV image pair by summing the square of the difference between the input and the output fields at each PIV interrogation window. The normalized standard deviations are determined as 5% for azimuthal velocity fields and 3% for vorticity fields. This value can be taken as an estimate of the experimental accuracy. However, it should be noted that the actual data contain out-of-plane motion, meaning that the axial velocity in the vortex wake carries particles through the light sheet. This loss of particles may introduce additional errors, which have not been accounted for in the above tests. Furthermore, the above analyses are performed on an isolated Lamb–Oseen vortex, while the experimental data consist of both one and two vortices that may not have the exact structure of a Lamb–Oseen vortex. The presence of another vortex may result in additional errors in aLPT. Another effect of the aLPT processing is that the algorithm underestimates the peak vorticity and overestimates the size of the vortex, due to its global filter settings chosen for processing, making it necessary to correct for this artificial increase in the vortex's dimensions. Further details on error analysis may be found in Bristol (2000) and Ortega (2001).

The flow field statistics for a given run are calculated for the entire field of view, as well as for the individual vortices. Post-processing is done using several codes written in IDL (Interactive Data Language of Research Systems, Inc.). Several integral quantities are used to characterize the whole wake, half-wake, or an individual vortex embedded in the wake. They are computed beginning with the first frame in which the vortices have formed. This takes one or two frames after the wing leaves the camera view. The analysis continues until the last frame in the run, or until the vortices leave the camera's field of view, or until a vortex can no longer be identified clearly. The two-dimensional output fields of aLPT (y, z) are cropped by 1 step along all four edges to remove the spurious values that exists along the border of the measurement domain. The integration is done over the whole data field when the whole wake or half-wake is imaged and the interest is in the total data field. When describing an individual vortex, the integration is done over the largest circular area that can be centred at the vorticity peak of that vortex without overlapping other vortices in the vicinity. The total circulation Γ_{tot} is obtained from

$$\Gamma_{tot} = \int \omega \, \mathrm{d}A, \tag{4.1}$$

which is also used to determine the circulation-based Reynolds number, $Re_\Gamma = \Gamma_{tot}/\nu$ for the wakes. The position of the vorticity centroid, $\boldsymbol{y}_\Gamma = (y_\Gamma, z_\Gamma)$, is obtained from from

$$\boldsymbol{y}_\Gamma = \frac{1}{\Gamma_{tot}} \int \boldsymbol{y}\omega \, \mathrm{d}A. \tag{4.2}$$

Note that $\boldsymbol{y}_\Gamma \to \infty$ when $\Gamma_{tot} \to 0$. To avoid the difficulties in describing the vorticity distribution when vorticity is not all of the same sign, we will use enstrophy ω^2. The total enstrophy EN is determined from

$$EN = \int \omega^2 \, \mathrm{d}A \tag{4.3}$$

and the position of the enstrophy centroid, $\boldsymbol{y}_{EN} = (y_{EN}, z_{EN})$, from

$$\boldsymbol{y}_{EN} = \frac{1}{EN} \int \boldsymbol{y}\omega^2 \, \mathrm{d}A. \tag{4.4}$$

For an equi-strength counter-rotating vortex pair, the enstrophy centroid is at the mid-point of the vortices while the vorticity centroid is at infinity. A measure of the dispersion of the vorticity field is desired. The dispersion radius of vorticity r_Γ, which is defined as

$$r_\Gamma^2 = \frac{1}{\Gamma_{tot}} \int |\boldsymbol{y} - \boldsymbol{y}_\Gamma|^2 \omega \, \mathrm{d}A, \tag{4.5}$$

may be considered an obvious candidate (Lamb 1938; Batchelor 1967). This measure works well when vorticity does not change sign over the region of interest. It causes difficulties, however, when vorticity changes sign. The dispersion radius r_Γ can become imaginary for $|\Gamma_{tot}| < \int |\omega| \, \mathrm{d}A$, and becomes undefined when $\Gamma_{tot} \to 0$. To avoid these difficulties, we use an *enstrophy dispersion radius* r_{EN} defined as

$$r_{EN}^2 = \frac{1}{EN} \int |\boldsymbol{y} - \boldsymbol{y}_{EN}|^2 \omega^2 \, \mathrm{d}A. \tag{4.6}$$

The enstrophy centroid defined in equation (4.4) is used to obtain finite values even when looking at a whole vortex wake where $\Gamma_{tot} \to 0$ and $\boldsymbol{y}_\Gamma \to \infty$. Note that $r_\Gamma = r_{EN}$ for a Rankine vortex and $r_\Gamma = \sqrt{2} r_{EN}$ for a Lamb–Oseen vortex. A pseudo-two-dimensional kinetic energy of the data field is calculated as

$$KE = \frac{1}{2} \int |\boldsymbol{v}|^2 \, \mathrm{d}A, \tag{4.7}$$

where $\boldsymbol{v} = (v, w)$. When vortices are aligned with the x-axis before instabilities amplify, the velocity field is nearly planar ($\boldsymbol{u} \approx (0, v, w)$), hence, equation (4.7) represents the true kinetic energy. KE is used as an indicator of the abrupt change from a nominally two-dimensional behaviour to a three-dimensional one. It does not capture the total kinetic energy of the flow field since substantial kinetic energy lies at large distances from the vortex cores.

In addition to calculating flow statistics for the entire wake, analyses are performed on the individual vortices. The vortex structure is obtained by fitting the circulation distribution of a Lamb–Oseen vortex,

$$\Gamma(r) = \Gamma_o (1 - \mathrm{e}^{-r^2/\sigma^2}), \tag{4.8}$$

to the circulation data of the vortices, where the radial coordinate r is measured from the vortex centroid. Note that $\sigma = r_\Gamma$. This fitting process is similar to that employed in figures 10 and 11 of Chen *et al*. (1999) and the fits have comparable scatter. With Γ_o and σ determined from the circulation fit, the vortices' core sizes can be found from

$$r_{max} = 1.12\sigma, \tag{4.9}$$

which is the radial location of maximum azimuthal velocity. The maximum azimuthal velocity is found by substituting r_{max} from equation (4.9) and Γ_o and σ from the fit of equation (4.8) into the azimuthal velocity distribution

$$u_\theta(r) = \frac{\Gamma_o}{2\pi r} (1 - \mathrm{e}^{-r^2/\sigma^2}). \tag{4.10}$$

The peak value of vorticity can also be found from Γ_o and σ by evaluating

$$\omega(r) = \frac{\Gamma_o}{\pi\sigma^2}\,\mathrm{e}^{-r^2/\sigma^2} \tag{4.11}$$

at $r = 0$. The advection velocity, $\boldsymbol{v}_c = (v_c, w_c)$, of a vortex is calculated by weighting the velocity field with the vorticity field as in Bilanin, Teske & Williamson (1977) and Marcus (1990) to give

$$\boldsymbol{v}_c = \frac{1}{\Gamma_o}\int \boldsymbol{v}\omega \mathrm{d}A. \tag{4.12}$$

Additionally, the kinetic energy of the vortices are obtained by employing equation (4.7) for the flap and tip vortices.

For the triangular-flapped wing, analysis of the flap and tip vortices continues until the instability gives rise to three-dimensional effects in the measurement plane. This criterion is somewhat subjective, because it depends on where the light sheet cuts the vortex wake. Typically, the flap and tip vortices are examined until there is a rapid change in their core sizes or until they begin to merge with each other. After this point, calculations for the individual vortices cease and the analysis continues only for those values computed over the entire field of view. For the rectangular wing, the vortices are examined over the entire run.

The integral quantities determined in equations (4.1–4.12) refer to instantaneous values in data fields. The average of an instantaneous integral value is calculated over a run and identified with an overbar $\overline{(\ )}$. Thus, $\Gamma(t)$ is the circulation at a PIV data field while $\overline{\Gamma}$ is the time average of $\Gamma(t)$ over a whole run or a part of a run when referring to an individual vortex. The subscripts t and f are used to identify the wing tip and the inboard tip of a triangular flap, respectively (figure 1). Also, the subscripts l and r are used to identify the left (port) and the right (starboard) side of the wings, respectively.

4.2. *Rectangular wing*

The PIV measurements for the rectangular wing, which are summarized in table 1, provide a comparison between the wake behaviour of a conventional wing and that of the triangular-flapped wings. For the eleven runs that were conducted with the rectangular wing, the measurements exhibit the highly two-dimensional steady nature seen in the flow visualization experiments. Changing the wing speed or angle of attack shifts the values of the measured quantities, but the general trends in the data remain unchanged.

4.2.1. *Vorticity contours and vortex trajectories*

Vorticity contours at several downstream distances are shown in figure 11 for Run PIV 11 in which $Re_\Gamma = 85\,600$. At $x/b = 0$, the tip vortices are rolling up from the vortex sheet generated by the wing, giving them an elongated shape. The initial separation distance between the left and right vorticity centroids is approximately 37 cm. The two counter-rotating vortices at the wing's centreline are due to either the boundary layer off the strut or corner vortices that form at the strut/wing junction. By 41 spans, the vortices have long since completed their roll-up process and are nearly circular in shape. Note that the left vortex is somewhat above the right vortex, which is a consequence of a slight asymmetry in the wing or strut construction. In the last two plots at $x/b = 83$ and 125, the vortices appear almost exactly as they do at $x/b = 41$ spans; the only difference is that they have descended further in the tank.

The trajectories of the individual left and right wing-tip vortices, as well as that

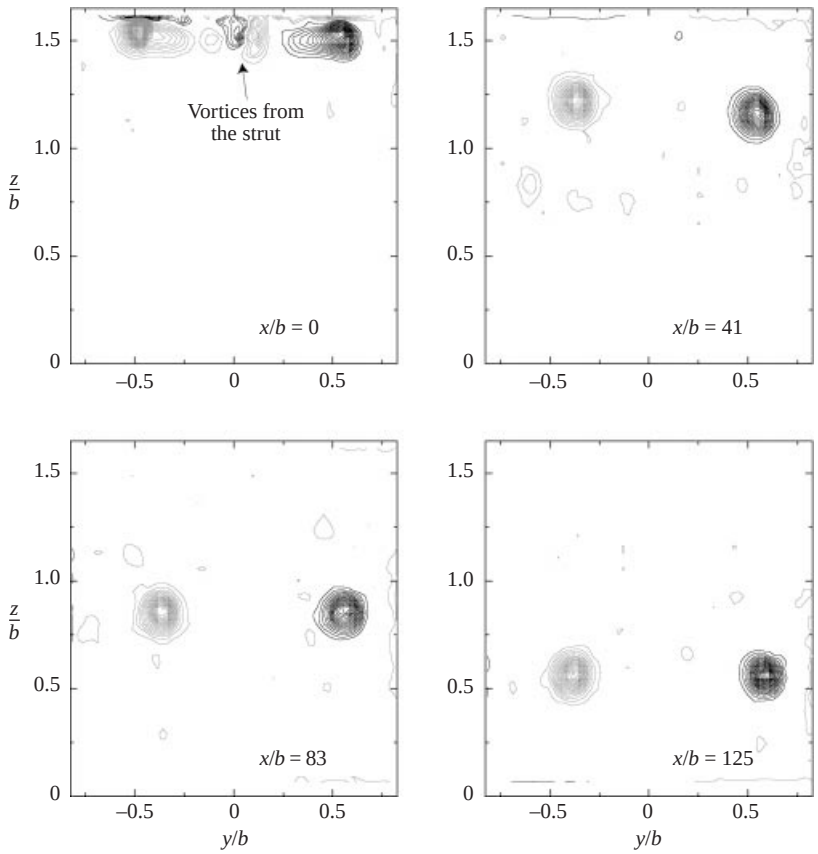

FIGURE 11. Vorticity contours at several downstream locations from the rectangular wing (Run PIV 11, $U_o = 500\,\mathrm{cm\,s^{-1}}$, $\alpha = 3°$). The black contours indicate positive values of vorticity and grey contours negative values. The same contour levels are used in each of the plots.

of the entire vortex wake, for Run 11 are shown in figure 12. The vorticity centroids of the left and right vortices are determined using equation (4.2) and are shown in figure 12(*a*). The enstrophy centroids of the left and right vortices as well as the whole wake are determined using equation (4.4) and shown in figure 12(*b*). The integration is taken over a rectangular area covering each vortex's respective half, extending from top to bottom and edge to centre of vorticity data such as those shown in figure 11. The enstrophy centroid of the whole wake is found through the integration over the enstrophy field of both vortices. The time histories of the enstrophy and vorticity centroids are also shown: the vertical positions in figure 12(*c*) and horizontal in 12(*d*). The individual vortex trajectories look nearly the same, especially the vertical time histories in figure 12(*c*) where five traces are plotted. Following the initial roll-up, the tip vortices descend vertically at nearly a constant rate for about one wing span. After about one wing span descent (about $x/b = 110$), the vortex trajectories seem to show signs of the effect of the bottom of the tank. The deviation of the trajectories from the fitted straight line in figure 12(*c*) at later times clearly shows that the descent wake of the wake, however measured, is decreasing. The separation distance of the vortices increases as seen in figure 12(*d*) and the vertical descent rate slows down, a clear indication that the affect of the image vortex system at tank bottom is coming into play. The enstrophy centroid of the whole wake, however, remains vertical due

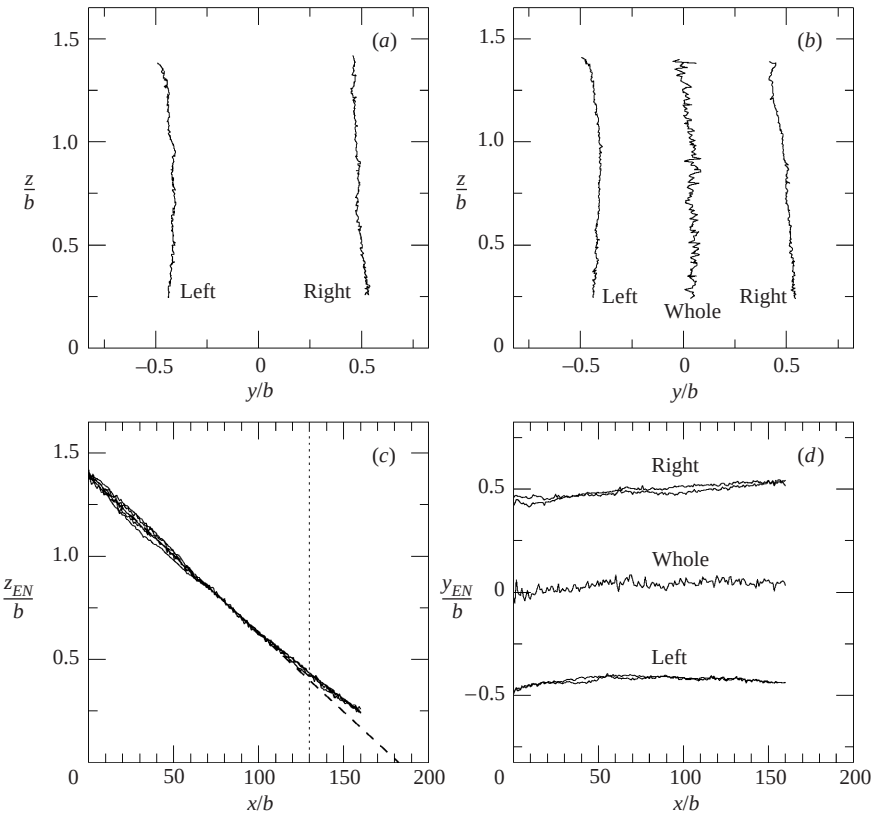

FIGURE 12. Vortex trajectories in the wake of the rectangular wing (Run PIV 11). (*a*) Paths of the vorticity centroids $\boldsymbol{y}_\Gamma$ of the left and right tip vortices. (*b*) Paths of the enstrophy centroids $\boldsymbol{y}_{EN}$ of the left and right tip vortices and the whole wake. (*c*) Vertical location, $z(t)$, for all paths in (*a*) and (*b*). The dashed line is a fit to $z_{EN}(t)$ for the whole wake for $x/b = [0, 110]$. (*d*) Horizontal location, $y(t)$, for all paths in (*a*) and (*b*).

to the wake symmetry (figures 12*b* and *d*). The nearly vertical paths of the vortices for the initial one-wing-span descent suggest that the PIV measurements within this descent region should be free of wall effects due to the tank bottom.

4.2.2. *Isovorticity surfaces*

One means of visualizing the vorticity data over an entire run is to plot an isovorticity surface, which is generated by stacking contours of one vorticity level for an entire run (Chen *et al.* 1999). Figures 13 and 14 show isovorticity surfaces for Run PIV 11. There are three isovorticity surfaces of $|\omega|$ shown in these two figures: $|\omega| = 9.5, 4.75$ and $2.85\,\mathrm{s}^{-1}$. These vorticity levels are chosen to be 25%, 12.5% and 7.5% of the maximum vorticity at $x/b = 0$. Figure 13 shows a side view of the isovorticity surfaces, such that the vertical axis in the plot is the z-direction. The cross-section of the wing displayed in the upper-left corner is intended to orient the reader. The horizontal axis is the downstream distance, x/b, from the wing. Figure 14 shows the same three isovorticity surfaces, but from a viewpoint of looking up at the wake from below. Again, the sketch of the wing in the upper left corner is placed there to orient the reader to the flow. Note that the vertical and lateral scales of these surfaces are equal to one another, but that the axial scale has been compressed.

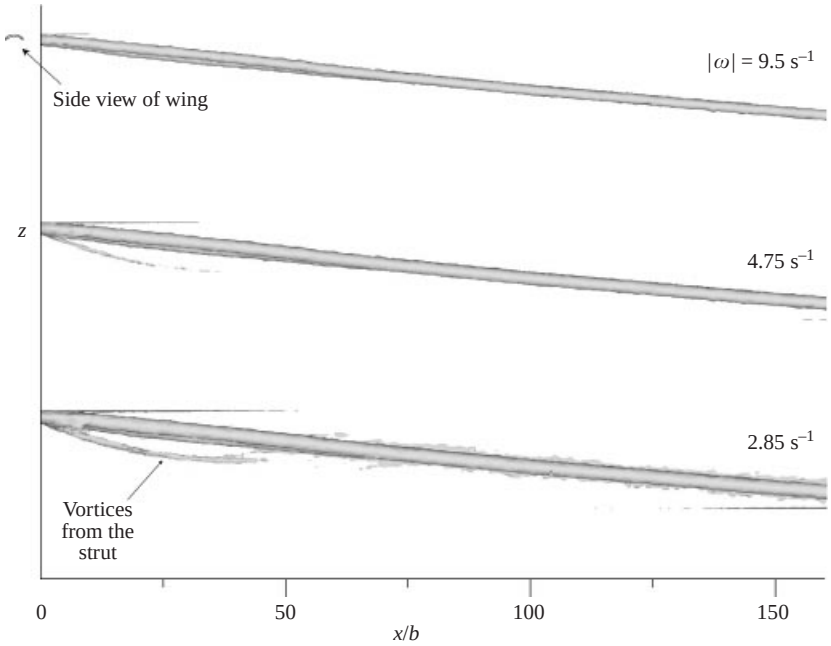

FIGURE 13. Side view of the isovorticity surfaces from the rectangular wing (Run PIV 11, $U_o = 500\,\mathrm{cm\,s^{-1}}$, $\alpha = 3°$). The horizontal axis is the downstream distance, x/b, from the wing.

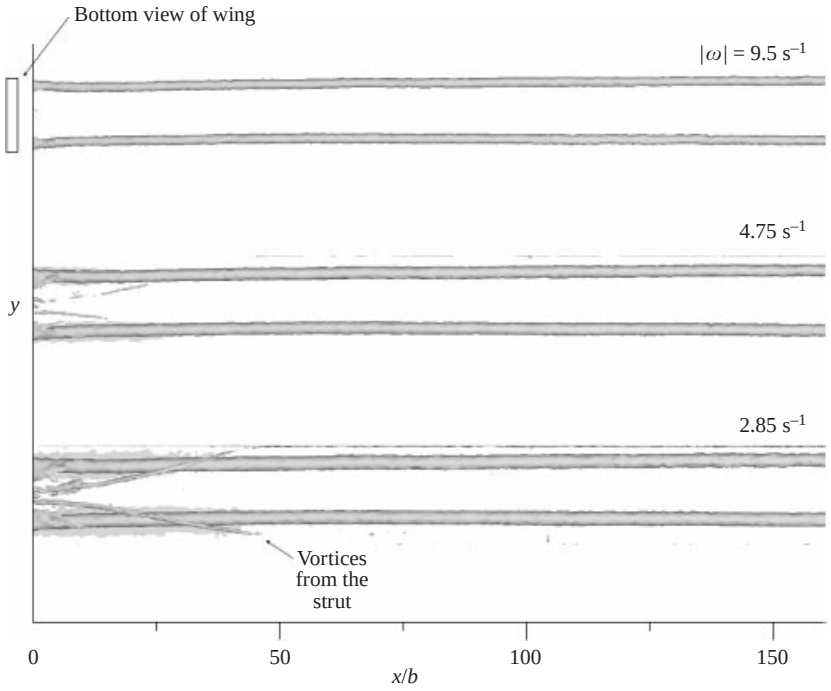

FIGURE 14. Bottom view of the isovorticity surfaces from the rectangular wing (Run PIV 11, $U_o = 500\,\mathrm{cm\,s^{-1}}$, $\alpha = 3°$). The horizontal axis is the downstream distance, x/b, from the wing.

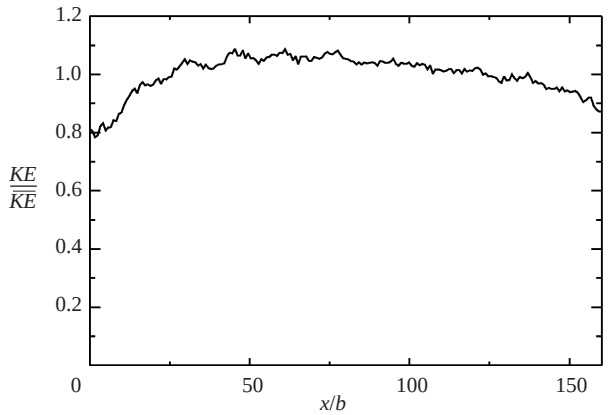

FIGURE 15. Two-dimensional kinetic energy as a function of downstream location for the rectangular wing (Run PIV 11). Note that $\overline{KE} = 2.55 \times 10^5\,\mathrm{cm}^4\,\mathrm{s}^{-2}$ and $x = U_o t$.

It can be seen in the side-view surfaces that the wake descends at a nearly constant rate over the entire run. The slight difference in the elevation of the right and left tip vortices is also evident in this view from $0 < x/b < 75$. The weaker counter-rotating vortex pair from the strut is evident in the side-view surfaces for $0 < x/b < 50$. The bottom view of the surfaces illustrates the initial roll-up of tip vortices. From $0 < x/b < 10$, the tip vortices move slightly inboard as the vortex sheet rolls up from the wing. Another important feature in figure 14 is the lateral positioning of the wake. Note that there are few, if any, oscillations in the spacing between the tip vortices. This indicates that there are no visible signs of developing instabilities and, consequently, the wake is uneventful.

4.2.3. *Two-dimensional kinetic energy*

The two-dimensional kinetic energy of the wake in Run PIV 11 is shown in figure 15. Equation (4.7) captures the true kinetic energy since the flow is nearly planar. The gradual rise and fall of the kinetic energy is due to the fact that the field of view does not encompass all of wake's kinetic energy. Therefore, the value of the kinetic energy depends upon the location of the vortices in the measurement plane. At $x/b = 0$ and 160, the vortices are at the top and bottom of the camera's view, so that only a portion of the kinetic energy is measured. However, at $x/b \approx 50$, the vortices are in the middle of the measurement plane, which results in a maximum value of the kinetic energy. These trends in the kinetic energy will later be compared with those of the triangular-flapped wings to highlight the three-dimensional nature of the instabilities.

4.2.4. *Vortex strength and structure*

The strength, Γ_o, and size, σ, of the vortices is measured by fitting their circulation distributions with that of a Lamb–Oseen vortex (equation (4.8)). Figure 16(*a*) displays the values of $\Gamma_o(t)$ as a function of the downstream distance from the wing. The circulation of the left vortex remains almost constant after the initial roll-up, while that of the right vortex experiences a slight decrease at $x/b = 160$. The vortex core sizes, $r_{max} = 1.12\sigma$, maximum azimuthal velocities, and peak vorticity values are shown in figure 16(*b–d*). All three of these variables have been computed with values of σ that have been corrected (§4.1) to remove the artificial increase in the vortex size from aLPT. The maximum azimuthal velocity is normalized by the wake's

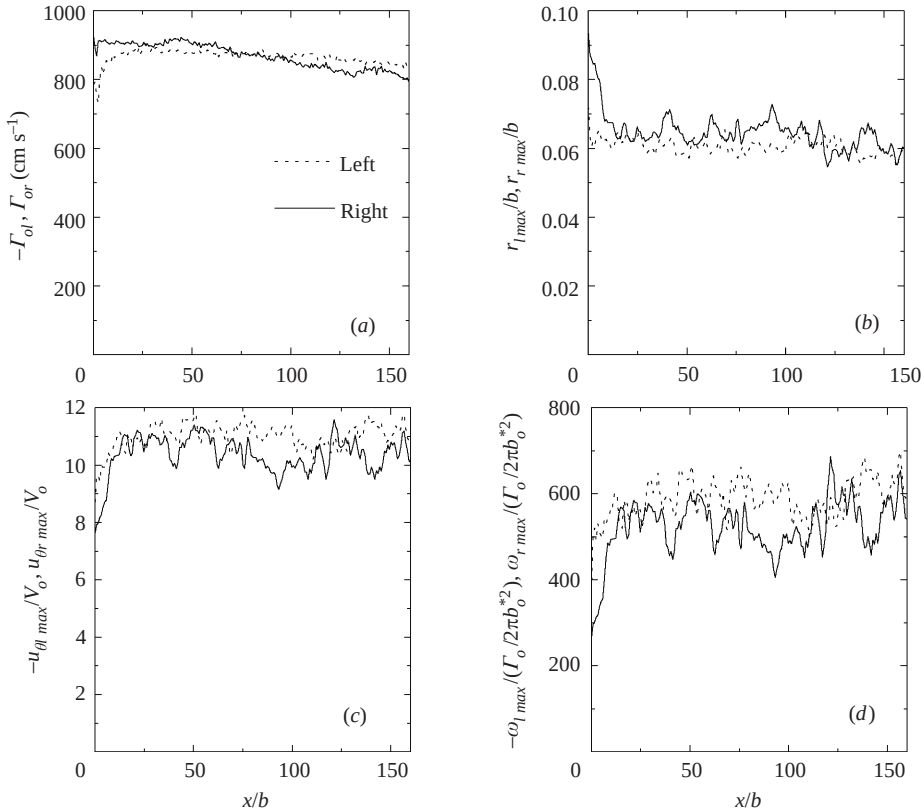

FIGURE 16. (*a*) Circulation, (*b*) vortex core sizes, (*c*) maximum azimuthal velocities, and (*d*) peak vorticity values as functions of downstream distance for the rectangular wing (Run PIV 11). The vortex core sizes, maximum azimuthal velocities, and peak vorticities have been computed with values of σ that are corrected to remove the artificial inflation by aLPT. $V_o = 3.71\,\mathrm{cm\,s^{-1}}$, $\Gamma_o(0)/2\pi b_o^{*2} = 0.1\mathrm{s}^{-1}$.

characteristic descent velocity, $V_o = \Gamma_o(0)/2\pi b_o^*$, where $\Gamma_o(0)$ is the average circulation of the left and right vortices at $x/b = 0$ and b_o^* is the initial separation of the left and right vorticity centroids. The peak vorticity is normalized by the reciprocal of the wake's characteristic descent time, $2\pi b_o^{*2}/\Gamma_o(0)$. The sizes of the right and left vortices vary only slightly about their average values of 6.4%b and 6.1%b. Because of the low temporal resolution of the PIV measurements, it is difficult to say if the small variations of the core sizes are caused by 'bulges' travelling through the laser sheet. The maximum azimuthal velocity and peak vorticity exhibit no measurable signs of decay over the run.

The PIV data from the wakes of the rectangular wing confirm the observations that were made previously from the flow visualization data. Namely, that the equal-strength counter-rotating vortex pairs evolve in a rather steady fashion with no evidence of bursting or decay. Similar trends were also seen in the wake of another rectangular wing at lower Re_Γ (Chen *et al.* 1999).

4.3. *Triangular-flapped wing*

The results of the triangular-flapped wing runs are shown in table 2. The properties of the wakes prior to the nonlinear effects of the instability were very repeatable.

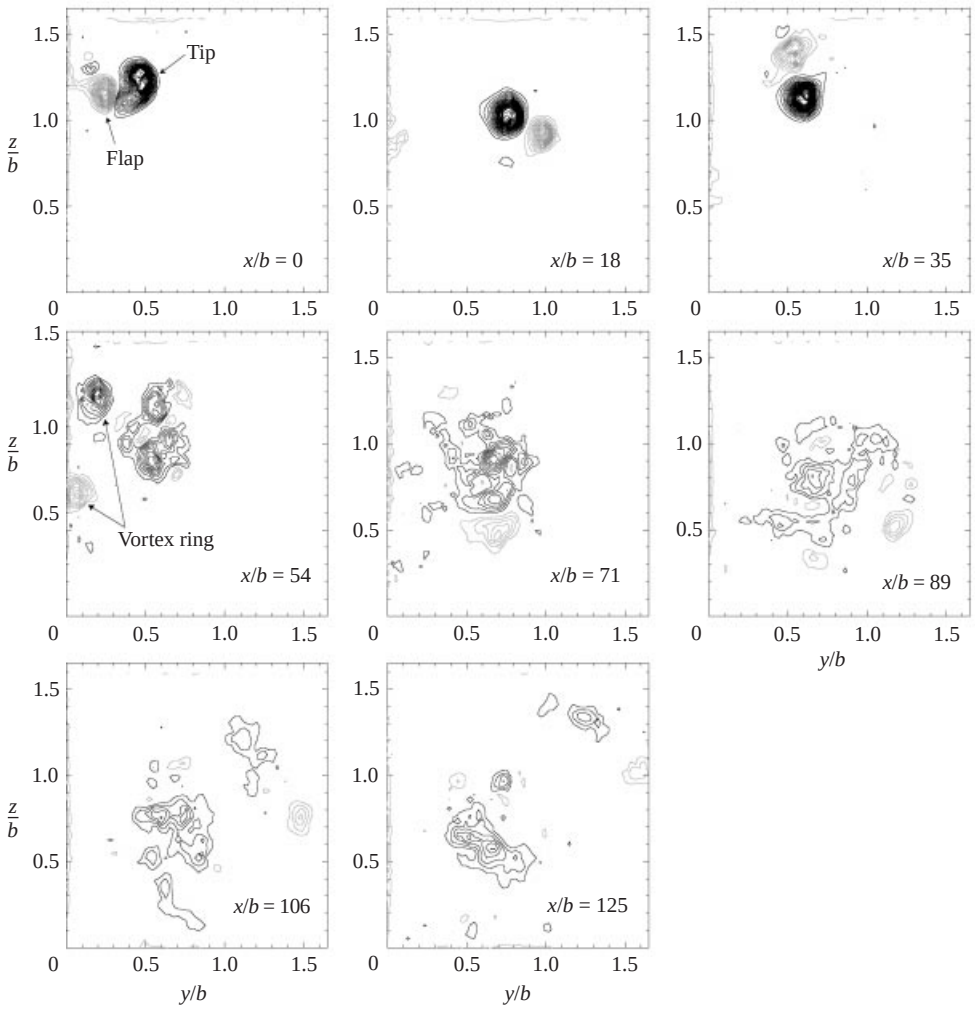

FIGURE 17. Vorticity contours at several downstream locations for $\overline{\Gamma}_{of}/\overline{\Gamma}_{ot} = -0.37$ (Run PIV 39, $U_o = 500\,\mathrm{cm\,s^{-1}}$, $\alpha = 2.0°$, 50%c TF). The black contours indicate positive values of vorticity and grey contours negative values. The same contour levels are used in each of the plots.

However, after the instability occurred, the unsteady, three-dimensional, and dynamic nature of these wakes quickly becomes evident in the PIV data. Consequently, the exact details of the flow at larger downstream distances vary from run to run.

4.3.1. *Vorticity contours and vortex trajectories*

The vorticity contours for a run in which $\overline{\Gamma}_{of}/\overline{\Gamma}_{ot} = -0.37$ (Run PIV 39, $U_o = 500\,\mathrm{cm\,s^{-1}}$, $\alpha = 2°$, 50%c TF) are shown in figure 17. Negative values of vorticity are labelled with grey contours and positive values with black contours. The same contour levels are used in all of the frames. At $x/b = 0$, the flap and tip vortices are rolling up from the wing. The 'comma'-like appearance of the tip vortex is due to the roll-up of the vortex sheet along the trailing edge of the triangular flap. The vorticity shed from the strut can also be seen on the left side of the plot from $1.2 < z/b < 1.6$. By 18 spans, the counter-rotating pair has orbited counter-clockwise around its common centroid by about $3\pi/4$ radians. From the flow visualization data,

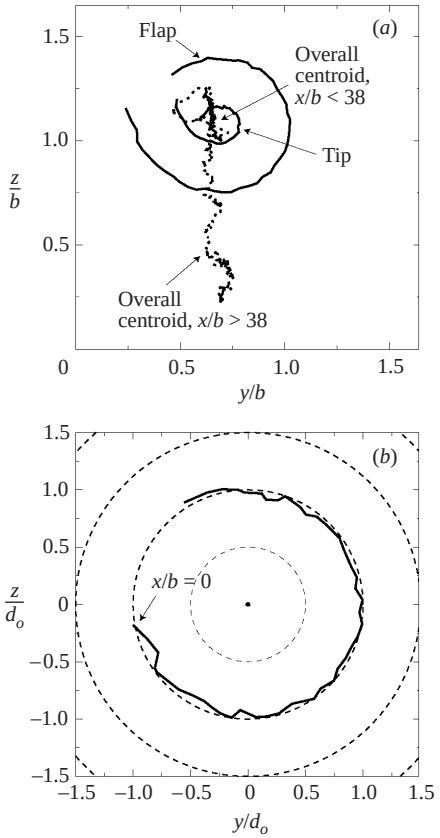

FIGURE 18. (*a*) Trajectories of the flap and tip vortices and overall centroid for $\overline{\Gamma}_{of}/\overline{\Gamma}_{ot} = -0.37$ (Run PIV 39, $U_o = 500\,\mathrm{cm\,s^{-1}}$, $\alpha = 2.0°$, 50%c TF). The thick, black line is the overall vorticity centroid for $0 \leqslant x/b < 38$ and the dotted line is the overall vorticity centroid for $x/b \geqslant 38$. (*b*) Position of the flap vortex with respect to the tip vortex for $0 \leqslant x/b < 38$.

the instability amplitude is finite at this downstream location, yet the vortices in this particular measurement plane exhibit no evidence of its presence. However, a rapid change in the vortices' core sizes occurs at 38 spans (not shown) as the nonlinear effects of the instability become evident in the measurement plane. At $x/b = 54$, the tip vortex splits into two and a vortex ring enters the measurement plane from the left. This ring collides with the right-side tip vortex at 71 spans, which results in large patches of vorticity being spread across the field of view. By 125 spans, a few remnant patches of vorticity remain, although their peak values are significantly less than those at $x/b = 0$.

The trajectories of the flap and tip vorticity centroids, as well as the centroid of the entire wake, are plotted for Run PIV 39 in figure 18(*a*) for $0 \leqslant x/b \leqslant 243$. Initially, the flap and tip vortices follow curved paths as they orbit outwardly about their vorticity centroid. The position of the flap vortex with respect to the tip vortex during this time is shown in figure 18(*b*). The flap vortex's position is normalized by the initial separation distance, d_o, between the flap and tip vortices, which for this run is 9.82 cm. It is evident that the distance between the vortices remains almost constant. For other runs, the distance between the flap and tip vortices increases or decreases, depending on whether or not the light sheet cuts the wake at a peak or trough of

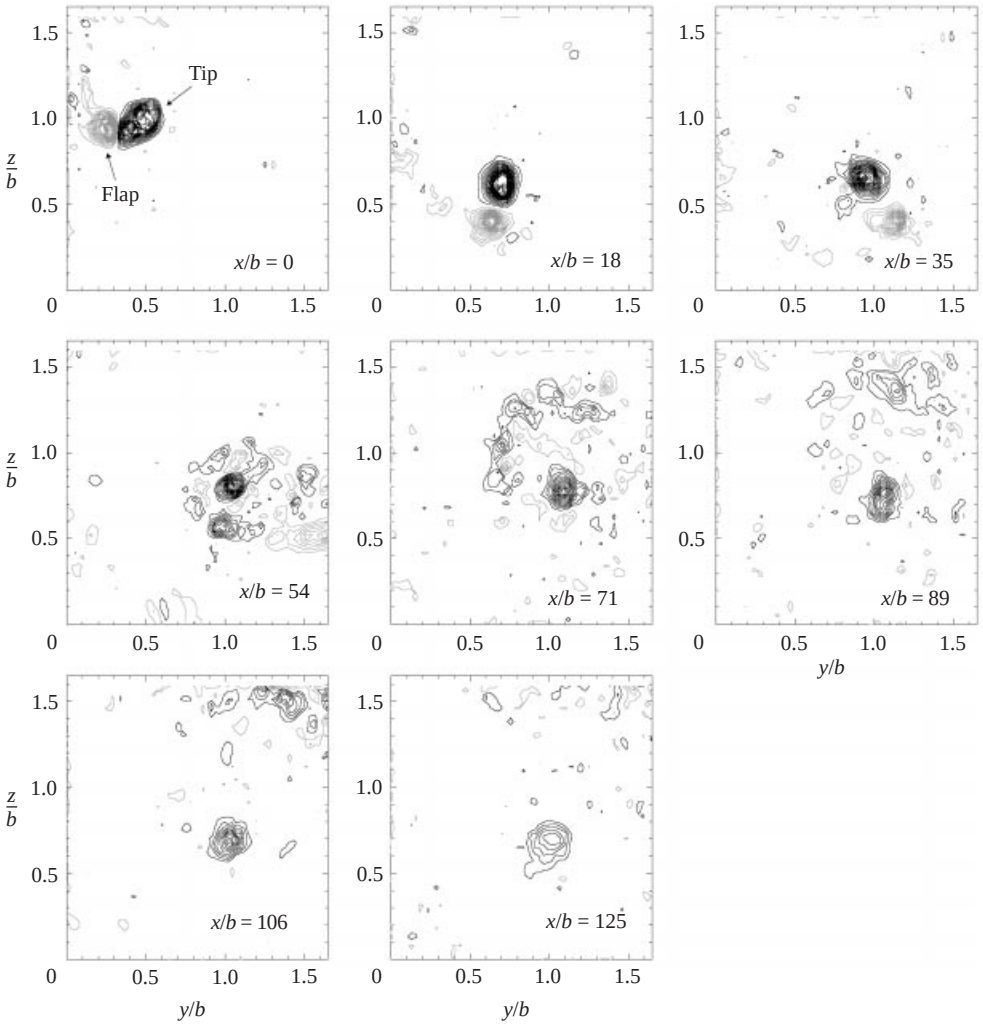

FIGURE 19. Vorticity contours at several downstream locations for $\overline{\Gamma}_{of}/\overline{\Gamma}_{ot} = -0.53$ (Run PIV 48, $U_o = 500\,\mathrm{cm\,s^{-1}}$, $\alpha = -1.0°$, 50%c TF wing). The black contours indicate positive values of vorticity and grey contours negative values. The same contour levels are used in each of the plots.

the instability on the flap vortex. While $x/b < 38$ spans, the wake's centroid descends vertically downward. However, as the vortex ring enters the field of view, the position of the wake's centroid fluctuates. After the collision of the ring and the tip vortex, the overall centroid continues its vertical descent.

For larger values of $|\overline{\Gamma}_{of}/\overline{\Gamma}_{ot}|$, the vortex dynamics appear somewhat different. Figure 19 illustrates this in the vorticity contours for a run in which $\overline{\Gamma}_{of}/\overline{\Gamma}_{ot} = -0.53$ (Run PIV 48, $U_o = 500\,\mathrm{cm\,s^{-1}}$, $\alpha = -1.0°$, 50%c TF). At $x/b = 54$, the tip vortex divides into smaller pieces and the flap vortex exits the measurement plane. In the subsequent contour plots, the sinusoidal instability results in an ejection of the flap vortex and its remnants towards the upper right-hand corner of the contour plots. Notice that there is no exchange of vorticity across the wing centreline. Instead, the nonlinear effects of the instability are confined to either side of the wake,

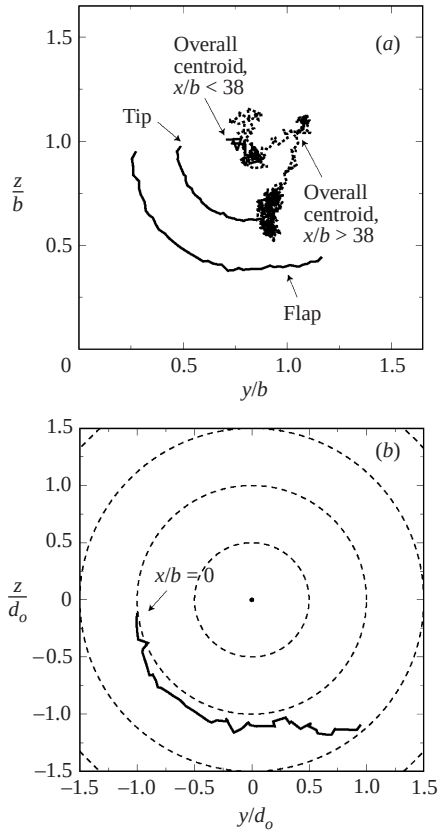

FIGURE 20. (*a*) Trajectories of the flap and tip vortices and overall centroid for $\overline{\Gamma}_{of}/\overline{\Gamma}_{ot} = -0.53$ (Run PIV 48, $U_o = 500\,\mathrm{cm\,s^{-1}}$, $\alpha = -1.0°$, 50%c TF). (*b*) Position of the flap vortex with respect to the tip vortex for $0 \leqslant x/b < 38$.

which is consistent with the flow visualization measurements discussed in § 3.2.2 (see figures 8–10).

The vortex trajectories for $\overline{\Gamma}_{of}/\overline{\Gamma}_{ot} = -0.53$ (figure 20) also differ from those of $\overline{\Gamma}_{of}/\overline{\Gamma}_{ot} = -0.37$ (Run PIV 39). As expected, the flap and tip vortices trace out circular arcs with larger radii, which is simply due to the fact that the vortices are more equal in strength. One interesting result is that the wake has a noticeably reduced descent velocity after the instability occurs. This phenomenon is mentioned above in the flow visualization observations (§ 3.2.2). In the flow visualization data, there appeared to be no distinct downwash in the test section for $x/b > 125$ (§ 3.2.2). However, because the dye was so dispersed at these downstream locations, no conclusions could be drawn from those images. The overall centroid of the wake, which is plotted up to 330 spans downstream of the wing, illustrates this observation. For $x/b > 38$, the overall centroid fluctuates greatly at first, but then lingers in the vicinity of the tip vortex's final location for the remainder of the run. This behaviour was consistently observed for the runs that had an angle of attack equal to $-1.0°$. Unlike the runs at $\alpha = 2°$, the overall centroid remains in approximately the same location for the remainder of the run and does not descend out of view. This is not to say that the wake has stopped descending completely. In fact, a review of the particle-streak data revealed that there is a small, but finite, amount downwash in the wake at 330 spans downstream of the wing.

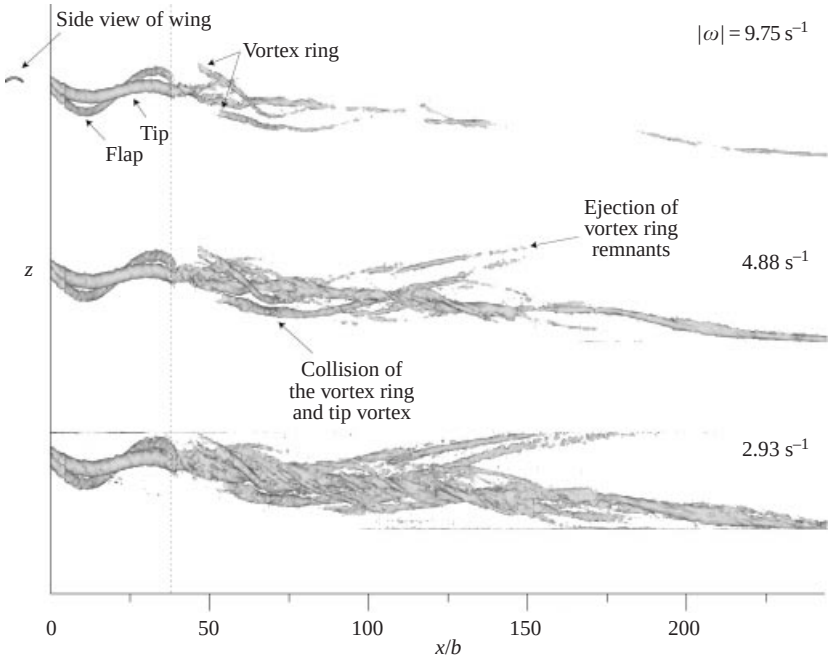

FIGURE 21. Side view of the isovorticity surfaces for Run PIV 39 ($U_o = 500\,\mathrm{cm\,s^{-1}}$, $\alpha = 2.0°$, 50%c TF, $\overline{\Gamma}_{of}/\overline{\Gamma}_{ot} = -0.37$). The horizontal axis is the downstream distance, x/b, from the wing.

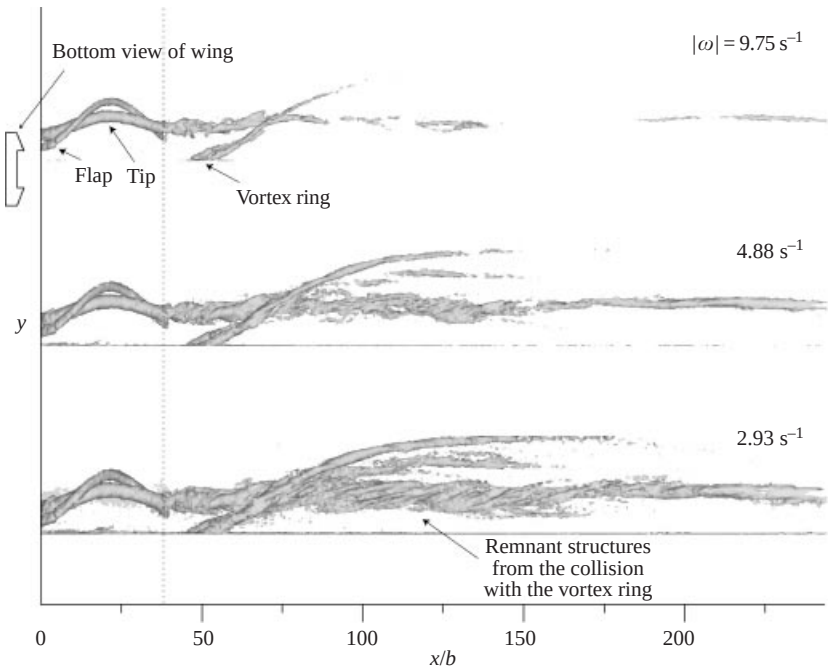

FIGURE 22. Bottom view of the isovorticity surfaces for Run PIV 39 ($U_o = 500\,\mathrm{cm\,s^{-1}}$, $\alpha = 2.0°$, 50%c TF, $\overline{\Gamma}_{of}/\overline{\Gamma}_{ot} = -0.37$). The horizontal axis is the downstream distance, x/b, from the wing.

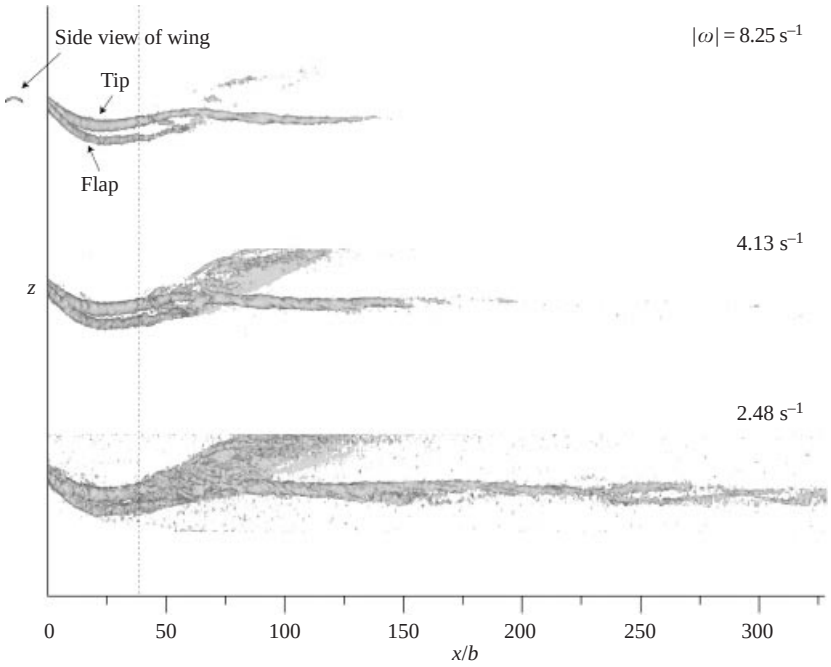

FIGURE 23. Side view of the isovorticity surfaces for Run PIV 48 ($U_o = 500\,\mathrm{cm\,s^{-1}}$, $\alpha = -1.0°$, 50%c TF, $\overline{\Gamma}_{of}/\overline{\Gamma}_{ot} = -0.53$). The horizontal axis is the downstream distance, x/b, from the wing.

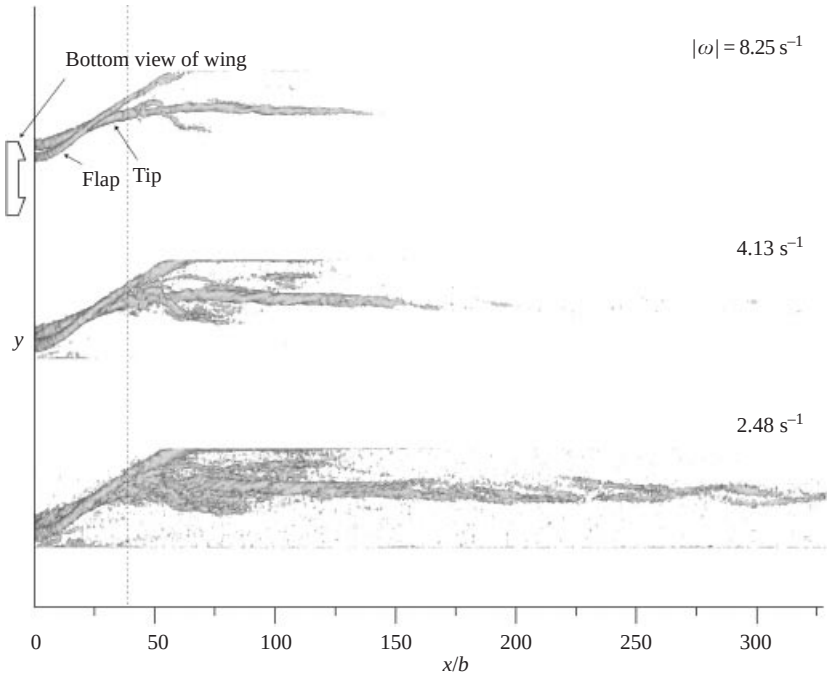

FIGURE 24. Bottom view of the isovorticity surfaces for Run PIV 48 ($U_o = 500\,\mathrm{cm\,s^{-1}}$, $\alpha = -1.0°$, 50%c TF, $\overline{\Gamma}_{of}/\overline{\Gamma}_{ot} = -0.53$). The horizontal axis is the downstream distance, x/b, from the wing.

Run PIV	Wing	U_o (cm s^{-1})	α (deg.)	$\Gamma_{tot.}(0)$ (cm^2 s^{-1})	$\overline{\Gamma}_{of}$ (cm^2 s^{-1})	$\overline{\Gamma}_{ot}$ (cm^2 s^{-1})	Re_Γ	$\overline{KE}$ (cm^4 s^{-2})	$\bar{r}_{tmax}/b$	$\bar{r}_{fmax}/b$
38	50%c TF	500	2	1009	−612	1644	100 900	164 000	0.069	0.039
39	50%c TF	500	2	1018	−607	1640	101 800	169 000	0.068	0.037
40	50%c TF	500	2	1073	−605	1663	107 300	165 000	0.068	0.034
42	50%c TF	500	0	570	−599	1228	57 000	94 500	0.066	0.044
43	50%c TF	500	0	602	−609	1237	60 200	79 200	0.061	0.045
44	50%c TF	500	0	641	−601	1237	64 100	93 000	0.063	0.044
46	50%c TF	500	−1	474	−597	1073	47 400	60 700	0.061	0.050
47	50%c TF	500	−1	549	−594	1053	54 900	65 600	0.060	0.052
48	50%c TF	500	−1	544	−576	1087	54 400	71 800	0.064	0.048
69	50%c TF	300	2	524	−396	980	52 400	70 500	0.071	0.044
70	50%c TF	300	0	335	−439	773	33 500	45 600	0.068	0.050
71	50%c TF	300	−1	239	−444	663	23 900	24 600	0.069	0.056
50	75%c TF	500	2	1051	−689	1705	105 100	150 000	0.069	0.036
52	75%c TF	500	2	1035	−699	1715	103 500	144 000	0.068	0.039
53	75%c TF	500	2	1019	−698	1719	101 900	133 000	0.071	0.039
55	75%c TF	500	0	670	−653	1276	67 000	107 000	0.063	0.042
56	75%c TF	500	0	652	−655	1306	65 200	97 000	0.063	0.040
57	75%c TF	500	0	620	−629	1266	62 000	82 100	0.061	0.040
59	75%c TF	500	−1	463	−649	1085	46 300	56 400	0.063	0.050
60	75%c TF	500	−1	490	−642	1114	49 000	60 500	0.064	0.053
61	75%c TF	500	−1	447	−650	1122	44 700	55 300	0.068	0.048
64	75%c TF	300	0	359	−453	796	35 900	32 000	0.068	0.050
65	75%c TF	300	−1	271	−408	655	27 100	22 200	0.066	0.063
66	75%c TF	300	2	591	−454	1012	59 100	72 500	0.071	0.045

TABLE 2. PIV run parameters for the triangular-flapped wings: 50%c TF wing; 75%c TF wing: $\Gamma_{tot.}(0)$, initial, total circulation; $\overline{\Gamma}_{of}$, average flap circulation; and $\overline{\Gamma}_{ot}$, average tip circulation. For other definitions see table 1.

4.3.2. *Isovorticity surfaces*

The isovorticity surfaces for Run PIV 39 ($U_o = 500\,\mathrm{cm\,s^{-1}}$, $\alpha = 2.0°$, 50%c TF, $\overline{\Gamma}_{of}/\overline{\Gamma}_{ot} = -0.37$) are shown in figures 21 and 22. The surfaces are shown for $|\omega| = 9.75$, 4.88, and $2.93\,\mathrm{s^{-1}}$, which correspond to 25%, 12.5%, and 7.5% of the maximum vorticity of the flap vortex at $x/b = 0$. Figure 21 shows a side view of these surfaces, while figure 22 shows the bottom view. The side view of the surfaces is taken from the vantage point located at the wing centreline and looking outboard to the triangular flap. Consequently, the flap vortex in figure 21 is initially closest to the viewer. The dashed line at $x/b = 38$ is the downstream distance at which the vortices exhibit a sudden change in their internal structure. Unlike the isovorticity surfaces for the rectangular wing (figures 13 and 14), the surfaces in the wake of the 50%c TF wing are highly unsteady and are characterized by large changes in the vorticity distribution. It is important to comment on how these figures are interpreted. If these two-dimensional data were the only information available about the wake, it would be nearly impossible to imagine that the flap vortices are undergoing a sinuous instability, which leads to the formation of vortex loops and rings. This clearly underscores the importance of the flow visualization data in this study. Therefore, the discussions in

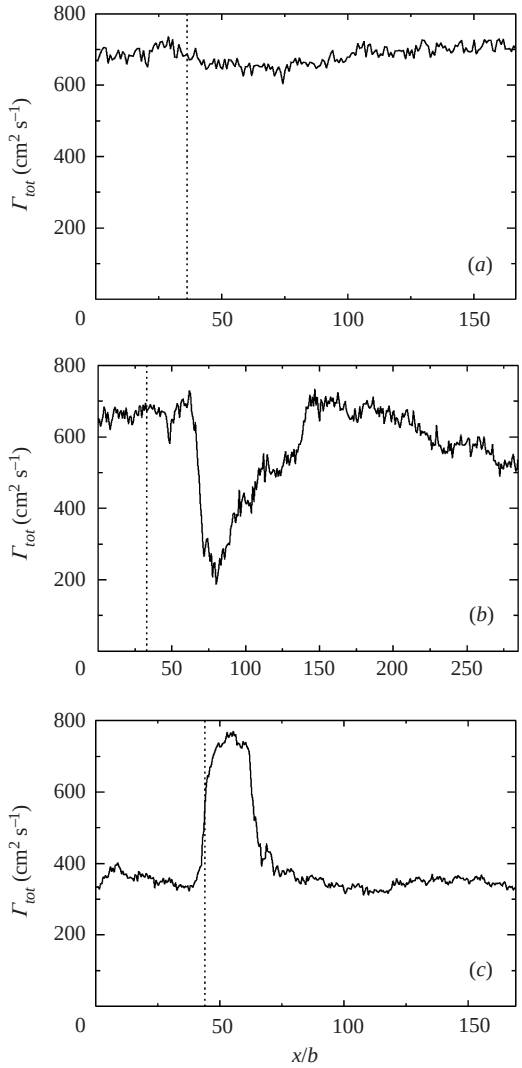

FIGURE 25. Various trends in the total circulation data. (*a*) Run PIV 55 (75%*c* TF, $\overline{\Gamma}_{of}/\overline{\Gamma}_{ot} = -0.51$). (*b*) Run PIV 56 (75%*c* TF, $\overline{\Gamma}_{of}/\overline{\Gamma}_{ot} = -0.50$). (*c*) Run PIV 70 (50%*c* TF, $\overline{\Gamma}_{of}/\overline{\Gamma}_{ot} = -0.57$). The vertical dashed lines denote the downstream distances at which the flap and tip vortices undergo a rapid change in their structure.

the following paragraphs are based upon both the PIV data and the flow visualization results.

For $x/b < 38$, the surfaces of the counter-rotating vortex pair are fairly smooth, indicating that the vorticity distribution is not varying significantly. At $x/b = 38$, the flap vortex seems to disappear from view. The reason for this is that the instability amplitude on the flap vortex has become finite, causing the flap vortex to tilt out of the measurement plane. Consequently, the PIV data no longer capture the flap vortex. Note that for $x/b \geqslant 38$, the isovorticity surfaces are no longer smooth, but are characterized by high-frequency events, demonstrating the unsteady, three-dimensional nature of the wake. At $x/b \approx 50$, the vortex ring from the opposite side of the wake enters the field of view and eventually collides with the remnant tip vortex.

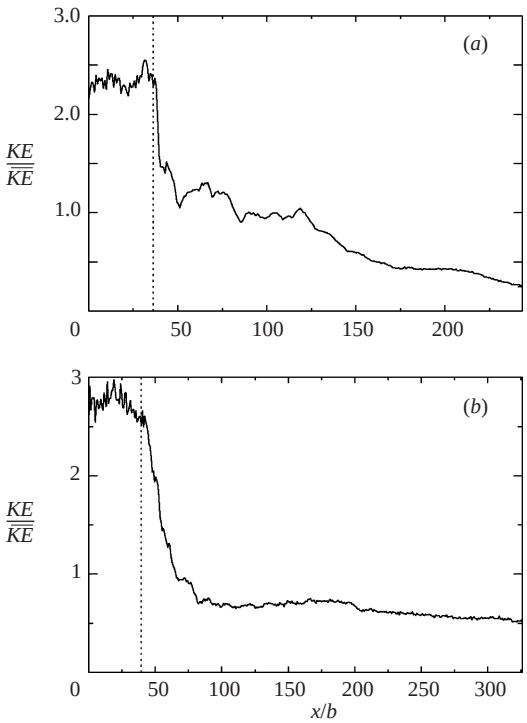

FIGURE 26. Two-dimensional kinetic energy as a function of downstream distance for the 50%c TF wing at small and large values of $|\overline{\Gamma}_{of}/\overline{\Gamma}_{ot}|$: (*a*) $\overline{\Gamma}_{of}/\overline{\Gamma}_{ot} = -0.37$, $\overline{KE} = 1.64 \times 10^5\,\mathrm{cm^4\,s^{-2}}$ (Run PIV 38, $U_o = 500\,\mathrm{cm\,s^{-1}}$, $\alpha = 2.0°$) (*b*) $\overline{\Gamma}_{of}/\overline{\Gamma}_{ot} = -0.56$ $\overline{KE} = 6.6 \times 10^4\,\mathrm{cm^4\,s^{-2}}$ (Run PIV 47, $U_o = 500\,\mathrm{cm\,s^{-1}}$, $\alpha = -1.0°$). The vertical dashed lines denote the downstream distance at which the flap and tip vortices undergo a rapid change in their core structures.

The details of this collision are quite interesting, as shown in figure 21. For this slice of the wake, the vortex ring is swept under the tip vortex and ejected upward out of the measurement plane. The top portion of the vortex ring interacts strongly with the tip vortex. The effects of this collision cause the formation of small-scale structures, which orbit about the tip vortex and give rise to the helical shapes in the $|\omega| = 2.93$ and $4.88\,\mathrm{s^{-1}}$ surfaces. The side view of the isovorticity surfaces demonstrates that for the remainder of the run, the wake, though highly disrupted, continues to descend in the test section.

The isovorticity surfaces for Run PIV 48 ($U_o = 500\,\mathrm{cm\,s^{-1}}$, $\alpha = -1.0°$, 50%c TF, $\overline{\Gamma}_{of}/\overline{\Gamma}_{ot} = -0.53$), which has a larger value of $|\overline{\Gamma}_{of}/\overline{\Gamma}_{ot}|$, are shown in figures 23 and 24. Again, these surface values correspond to 25%, 12.5% and 7.5% of the maximum vorticity of the flap vortex at $x/b = 0$. Note that the horizontal scale for Run PIV 48 is different than that of Run PIV 39. The dashed line at $x/b = 38$ denotes the downstream distance at which a sudden change is seen in the vortices' internal structure. For $x/b \geqslant 38$, the tip vortex becomes shrouded with a cloud of small-scale structures as the nonlinear effects of the instability propagate through the measurement plane. As discussed § 4.3.1, the sinusoidal instability on the flap vortex leads to the ejection of the flap vortex from the field of view at $x/b \approx 75$.

One of the more noticeable features in figures 23 and 24 is the reduction of the vorticity magnitude. For $x/b \geqslant 150$, the vorticity magnitude drops below a value of $8.25\,\mathrm{s^{-1}}$. Furthermore, for $x/b \geqslant 200$, only a few small patches of vorticity have

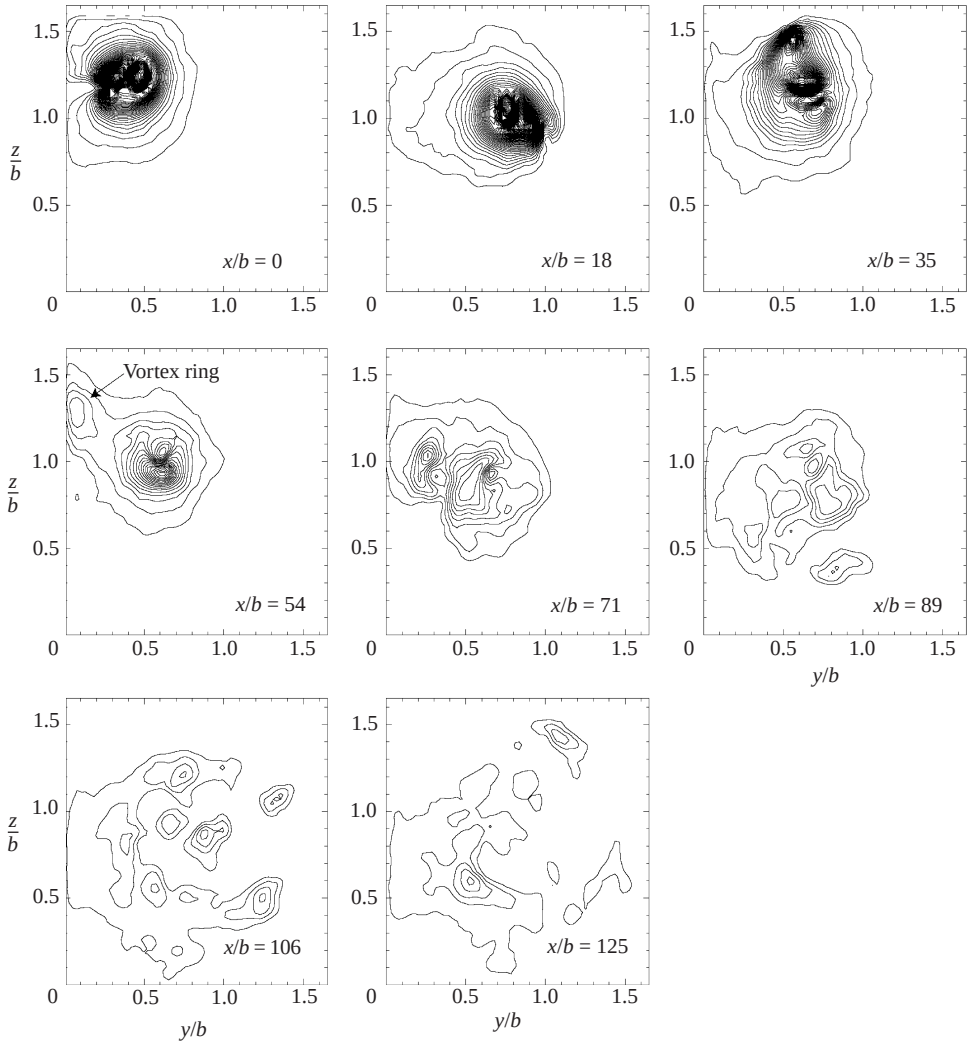

FIGURE 27. Contours of the two-dimensional kinetic energy for $\overline{\Gamma}_{of}/\overline{\Gamma}_{ot} = -0.37$ (Run PIV 38, $U_o = 500\,\mathrm{cm\,s^{-1}}$, $\alpha = 2.0°$, 50%c TF). The same contour levels are used in each of the plots.

magnitudes equal to $4.13\,\mathrm{s^{-1}}$. The descent characteristics of Run PIV 48 can also be seen in the side view of the isovorticity surfaces. The data in figure 23 show the reduced descent velocity of the wake after the instability has occurred. By 330 spans, the few remnant patches of the tip vortex are only slightly below the depth of the tip vortex at $x/b = 100$.

4.3.3. *Circulation budget*

After viewing the flow visualization and isovorticity surface data of the counter-rotating pairs, one question that arises is whether or not the circulation is conserved in the PIV measurement plane. For the case of the rectangular wing, the answer is a straightforward yes. The vortices behave nearly two-dimensionally. The PIV measurement plane intersects the vortices almost orthogonally. When the circulations for each tip vortex are calculated in figure 16(*a*), the integration region in equation (4.1) is sufficiently large that no appreciable vorticity is present at or near the boundaries.

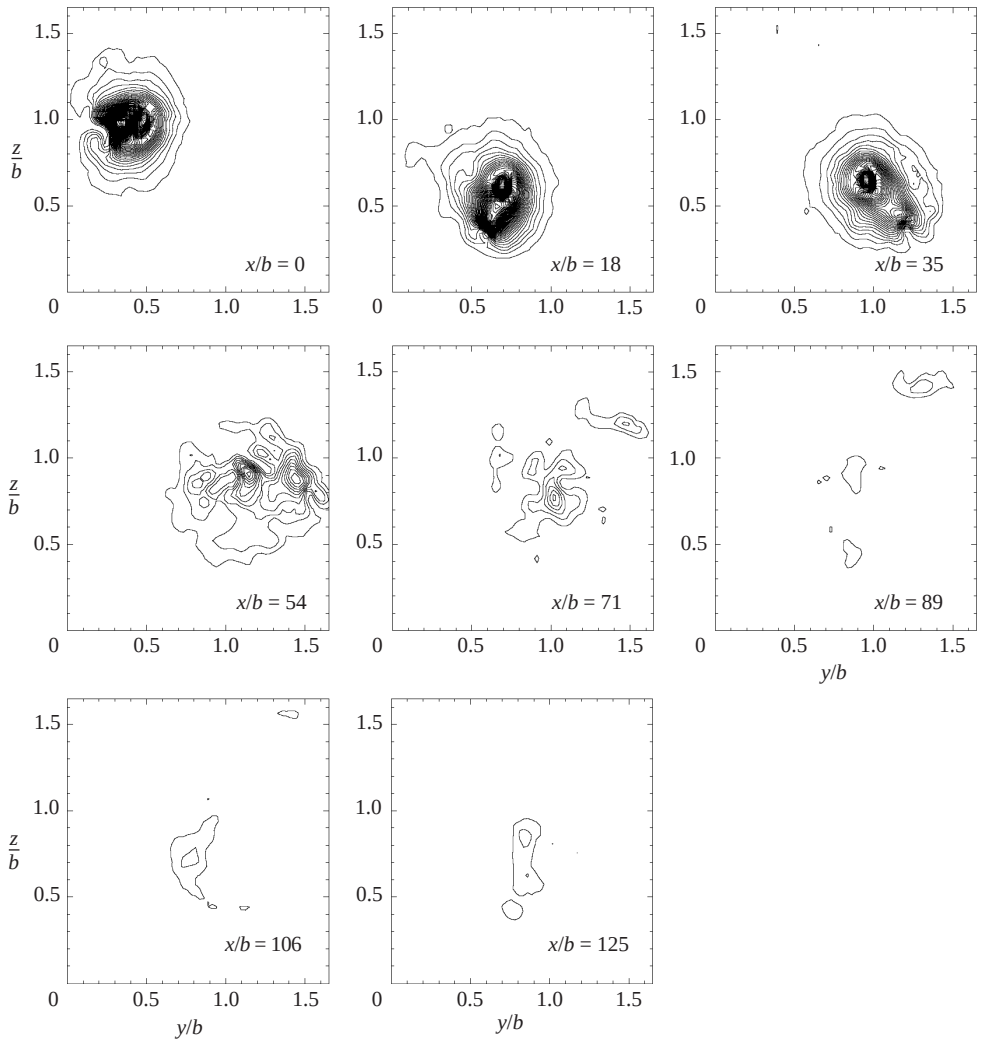

FIGURE 28. Contours of the two-dimensional kinetic energy for $\overline{\Gamma}_{of}/\overline{\Gamma}_{ot} = -0.56$ (Run PIV 47, $U_o = 500\,\mathrm{cm\,s^{-1}}$, $\alpha = -1.0°$, 50%c TF). The same contour levels are used in each of the plots.

There is no exchange of vorticity between the two sides of the wing. The vortex cores do not show any sign of significant growth to spread vorticity. Essentially, the integration is equivalent to the determination of circulation using a closed material contour that is sufficiently far away from vortical regions as required by the Kelvin circulation theorem (Saffman 1992). Therefore, within experimental uncertainty, circulation of each vortex remains constant as seen in figure 16(a).

The situation is quite different in the wakes of the flapped wings where the instability develops, grows, and alters the wake vortex filament topology. For some runs, the circulation in the PIV measurement plane does remain relatively constant and in others it changes radically. The reason for this behaviour is that the PIV plane is fixed. The instabilities, as nearly as we can observe, are also fixed in the laboratory reference frame. The relative position of the PIV plane with respect to an instability wave cycle, however, is arbitrary. This is due to the random starting point

of the carriage during towing, variations in growth rates and other factors that differ among the experimental runs. The PIV measurement plane can no longer serve as a surrogate for a closed material contour enveloping a vortex filament. Vorticity is exchanged between the two halves of the wing. Flow visualization pictures show the distinct change in the topology of the vortex filaments. They undulate, twist, connect and reconnect radically. It is even conceivable that a filament can bend without connection or reconnection and make multiple entries into the PIV measurement plane, even though none has been observed here. Hence, depending on where the PIV measurement plane intersects an instability cycle, the total circulation in the PIV plane can show seemingly unpredictable, even impossible behaviour. In such cases, a knowledge of the three-dimensional behaviour is necessary for correct interpretation.

Three examples are shown in figure 25. Figure 25(*a*) for Run PIV 55 ($U_o = 500\,\mathrm{cm\,s^{-1}}$, $\alpha = 0^\circ$, 75%c TF, $\overline{\Gamma}_{of}/\overline{\Gamma}_{ot} = -0.51$) shows a case where the total circulation remains nearly constant. The dashed line at $x/b = 36$ denotes the downstream location at which a sudden change occurs in the vortices' core structures. It is evident that the circulation decreases a small amount after 36 spans, though in general the circulation varies only slightly about its initial value of $670\,\mathrm{cm^2\,s^{-1}}$. This is comparable to the flow visualized in figures 9 and 10 where there is no evidence of vorticity exchange between the opposite sides of the wing and all vortical activity that begins in the PIV plane remains there.

The circulation can fluctuate strongly for some other runs, such as that shown in figure 25(*b*) for Run PIV 56 ($U_o = 500\,\mathrm{cm\,s^{-1}}$, $\alpha = 0^\circ$, 75%c TF, $\overline{\Gamma}_{of}/\overline{\Gamma}_{ot} = -0.50$). Although the wing speed and angle of attack are identical to those of Run PIV 55, the trends in the circulation plot are completely different. At 75 spans, the circulation abruptly decreases by approximately 70%, which might give the impression that the circulation in the wake is suddenly decaying. However, this is not the case. The reason for the rapid 'decay' in the wake's circulation is that the measurement plane does not contain all of the wake's vorticity. As the flap and tip vortices on both sides of the wake undergo their cooperative instabilities, vortex loops and rings enter and exit the field of view, causing the measured circulation to vary strongly. In this particular run, a vortex ring, which originates from the left flap vortex, enters the top of the measurement plane so that only the 'negative' portion of the ring is imaged. Consequently, the 'total' circulation plummets due to this additional negative vorticity. Notice that the circulation drops by a value comparable to the flap's circulation (table 2). From 75 to 150 spans, the circulation steadily increases as the 'positive' portion of the vortex ring enters the field of view and cancels its 'negative' vorticity. By 150 spans, the circulation returns to a value close to that at $x/b = 0$. Over the rest of the run, the circulation decreases more slowly as more and more of the vorticity is ejected from the field of view.

Another example of a wake in which the circulation in the measurement plane is not constant is shown in figure 25(*c*) for Run PIV 70 ($U_o = 500\,\mathrm{cm\,s^{-1}}$, $\alpha = 0^\circ$, 50%c TF, $\overline{\Gamma}_{of}/\overline{\Gamma}_{ot} = -0.57$). The measurement plane for this run intersects the flap's sinusoidal instability at a local peak, such that the observed distance between the flap and tip vortices increases as the instability evolves. Eventually, the instability amplitude grows so large that the flap vortex exits the field of view at 44 spans, resulting in an increase in 'total' circulation. By 75 spans, the flap vortex and its remnants re-enter the measurement plane and the circulation decreases to a value comparable to that at $x/b = 0$. For the remainder of the run, no vortex rings enter or exit the measurement plane and the circulation remains relatively constant.

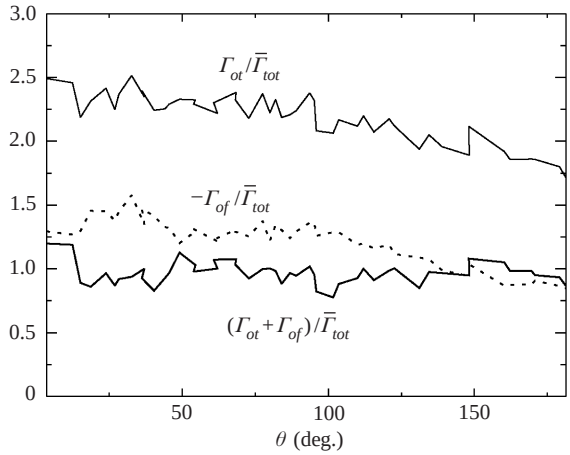

FIGURE 29. Circulation of the flap and tip vortices as a functions of orbit angle, θ, prior to the nonlinear effects of the instability for Run PIV 46 ($U_o = 500\,\mathrm{cm\,s^{-1}}$, $\alpha = -1.0°$, 50%c TF).

From these widely varying trends in the circulation data, it is difficult to conclude whether or not the flow is behaving inviscidly as the instability progresses. Viscous effects are certainly occurring in the vortex reconnection and collision processes, but given the large Re_Γ of these vortices, the viscous effects are too small to be a dominant factor in the evolution of these wakes. One trend evident over the entirety of some runs (Run PIV 55) or portions of others (Run PIV 70 for $75 \leqslant x/b \leqslant 170$) is that if no vorticity enters or exits the measurement plane, the circulation stays about constant, as dictated by Helmholtz's laws of vortex motion. These observations underscore the necessity of three-dimensional information for correct physical interpretation.

4.3.4. *Two-dimensional kinetic energy of the wake*

Perhaps one of the more interesting integral quantities measured in the wakes of the triangular-flapped wings is the two-dimensional kinetic energy KE in equation (4.7). In § 4.2.3, it was shown that this quantity changes relatively slowly in the wake of the rectangular wing (figure 15). However, given the highly three-dimensional wake of the triangular-flapped wings, we expect that KE will vary strongly with downstream distance. Indeed, this is the case as figure 26(a) illustrates for Run PIV 38 ($U_o = 500\,\mathrm{cm\,s^{-1}}$, $\alpha = 2.0°$, 50%c TF, $\overline{\Gamma}_{of}/\overline{\Gamma}_{ot} = -0.37$). Prior to about 35 spans (vertical dashed line), KE changes only slightly as the counter-rotating pair traverses the first three-quarters of its orbit period. Although the flow visualization shows that the instability becomes finite at about 25 spans, the kinetic energy does not give an obvious indication of its presence at that downstream location. However, at about 35 spans, KE decreases by about 30% as the flap vortex is tilted in the measurement plane by the instability. Consequently, the planar PIV measurements can no longer capture the flap vortex's true kinetic energy. Therefore, the drop in KE is primarily due to the tilting of the flap vortex. Further decrease in KE is, perhaps, due to either a disruption of the tip vortex's coherence or a slight tilting of the tip vortex in the field of view. At approximately 50 spans, a vortex ring enters the measurement plane from the opposite side of the wake and impacts the tip vortex. Over the rest of the run, the wake's kinetic energy continues to decay slowly.

To illustrate the distribution of KE in the wake, figure 27 shows contours of kinetic energy for Run PIV 38 ($U_o = 500\,\mathrm{cm\,s^{-1}}$, $\alpha = 2.0°$, 50%c TF). The same contour levels

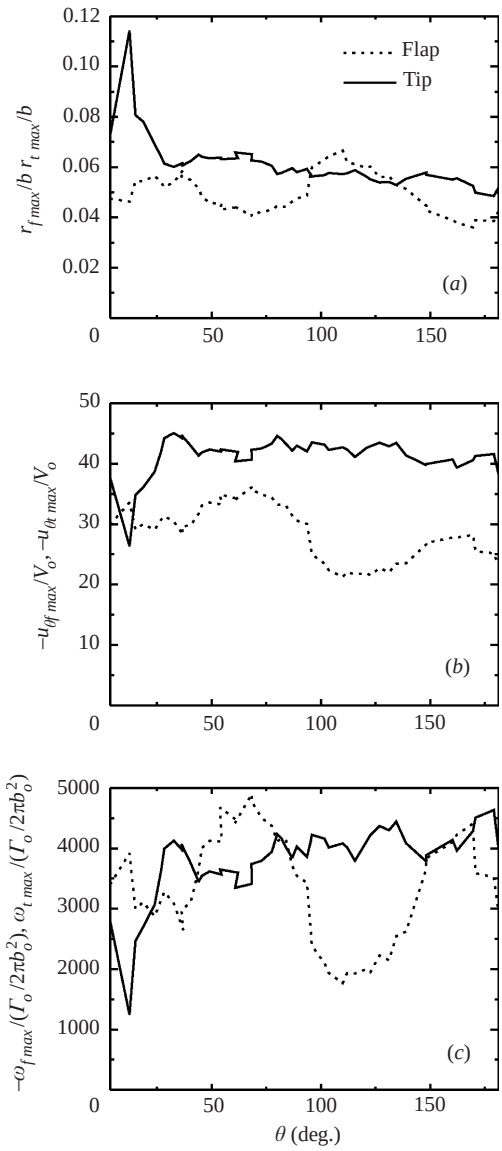

FIGURE 30. (*a*) Vortex core size, (*b*) maximum azimuthal velocity, and (*c*) peak vorticity of the flap and tip vortices as a function of orbit angle, θ, for Run PIV 46 ($U_o = 500\,\mathrm{cm\,s^{-1}}$, $\alpha = -1.0^\circ$, 50%c TF). Note that these plots are based upon values of the vortex core size, σ, that have been corrected to remove the artificial inflation from aLPT. $V_o = 1.23\,\mathrm{cm\,s^{-1}}$, $\Gamma_o(0)/2\pi b_o^2 = 0.2\,\mathrm{s^{-1}}$.

are used in all of the plots. As the vortices roll up at $x/b = 0$, the kinetic energy has a compact distribution around the counter-rotating pair. At 54 spans, a vortex ring enters from the opposite side of the wake and the kinetic energy associated with it is visible on the left side of the contour plot. The vortex ring begins to collide with the remnants of the tip vortex at 71 spans, which subsequently spreads the kinetic energy over a large region of the measurement plane. For larger downstream locations, the peak values in the kinetic energy are markedly lower than those in the contour plots prior to 36 spans.

For larger values of $|\overline{\Gamma}_{of}/\overline{\Gamma}_{ot}|$, the trends in two-dimensional kinetic energy are somewhat different than those described above, regardless of Re_c. Figure 26(b) demonstrates this for a run in which $\overline{\Gamma}_{of}/\overline{\Gamma}_{ot} = -0.56$ (Run PIV 47, $U_o = 500\,\mathrm{cm\,s^{-1}}$, $\alpha = -1.0°$, 50%c TF). One immediate difference between the kinetic energy of runs 38 and 47 is that the kinetic energy in Run PIV 47 experiences a larger relative drop when the instability becomes evident at 40 spans. Before 40 spans, the flap vortex makes up about 20% of the flow's kinetic energy. However, the total kinetic energy decreases by approximately 70%, not 20%. Consequently, the drop in kinetic energy is not just due to the tilting of the flap vortex in the measurement plane. The additional decrease in the kinetic energy arises from the tilting and disruption of the tip vortex. This tilting is visible in the flow visualization data for the right-hand tip vortex in figure 10 at $x/b = 50$. Over the rest of the run, the kinetic energy in figure 26(b) does not decrease as much as it does in Run PIV 38. Rather, the value of the kinetic energy at 100 spans is close to its final value at 326 spans. Figure 28 displays contours of two-dimensional kinetic energy for Run PIV 47. Initially, the distribution of kinetic energy appears similar to that of Run PIV 38. However, as the instability progresses, less and less of the two-dimensional kinetic energy is present in the field of view. By 125 spans, the contour plot displays only a patch of kinetic energy, which is noticeably smaller than that of Run PIV 38 at the same downstream location.

The trends in KE described above are consistently observed in the PIV data for both the 50%c and 75%c triangular-flapped wings. When the instability first becomes evident in the measurement plane, the two-dimensional kinetic energy always drops by a significant amount, regardless of $\overline{\Gamma}_{of}/\overline{\Gamma}_{ot}$. However, the residual decay of the kinetic energy does depend on $\overline{\Gamma}_{of}/\overline{\Gamma}_{ot}$. For larger values of $|\overline{\Gamma}_{of}/\overline{\Gamma}_{ot}|$, the kinetic energy does not decrease appreciably after its initial drop, as was shown above for Run PIV 47 in figure 26(b). Alternatively, for runs in which $|\overline{\Gamma}_{of}/\overline{\Gamma}_{ot}|$ is relatively small, like Run PIV 38, the kinetic energy continues to decay. There are a few reasons for this difference in decay characteristics. First, for the runs that have smaller values of $|\overline{\Gamma}_{of}/\overline{\Gamma}_{ot}|$, the instability leads to an exchange of vorticity from opposite sides of the wake. As the instability evolves, the flap vortices form coherent Ω-loops. The vortex rings that form from these loops have cross-sections that are coherent and comparable in size to the original flap vortices. Although these rings are three-dimensional in nature, they contribute considerably to the two-dimensional kinetic energy calculation in equation (4.7). Therefore, when they cross the wing centreline, the rings contribute to the total kinetic energy. As these rings collide and interact with the tip vortices, the flow becomes increasingly three-dimensional and the two-dimensional kinetic energy slowly decays. For larger values of $|\overline{\Gamma}_{of}/\overline{\Gamma}_{ot}|$, the nonlinear behaviour of the instability is confined to the opposite sides of the wake and there is little exchange vorticity across the wing centreline.

The second reason is due to the relative strengths of the flap and tip vortices. For runs in which $|\overline{\Gamma}_{of}/\overline{\Gamma}_{ot}|$ is small, the initial behaviour of the instability does not significantly affect the tip vortex simply because it is much stronger than the flap vortex. As the flap vortex forms Ω-loops that pinch off into rings, the tip vortex does not tilt significantly in the measurement plane. This is evident in the flow visualization images in figures 5 ($x/b = 28, 32$) and 6 ($x/b = 25, 36$) for a run in which $\overline{\Gamma}_{of}/\overline{\Gamma}_{ot} = -0.37$. As a result, a considerable amount of KE due to the tip vortex remains in the field of view. This nearly two-dimensional flow slowly becomes more three-dimensional over the rest of the run for the reasons explained above. However, for runs in which $|\overline{\Gamma}_{of}/\overline{\Gamma}_{ot}|$ is relatively large, the initial nonlinear behaviour

affects not only the two-dimensional kinetic energy of the flap vortex, but also that of the tip vortex. Since the two vortices are more comparable in strength, the finite-amplitude perturbations tilt and disrupt both the flap and tip vortices, causing a large drop in the wake's two-dimensional kinetic energy. The flow is so three-dimensional over the rest of the run that the two-dimensional kinetic energy remains at a small fraction of its initial value.

4.3.5. *Vortex structure*

The structure and behaviour of the individual flap and tip vortices are analysed in a manner similar to that of the rectangular wing. Consider Run PIV 46 ($U_o = 500\,\mathrm{cm\,s^{-1}}$, $\alpha = -1.0°$, 50%c TF) in which $\overline{\Gamma}_{of}/\overline{\Gamma}_{ot} = -0.56$. The circulations of the flap and tip vortices are plotted in figure 29 against the orbit angle θ over the first half of the orbit period, corresponding to the first 40 spans downstream of the wing. The orbit angle θ of the vortex pair is measured counter-clockwise from the plane of the wing. For $\theta > \pi$, the wake displays three-dimensional behaviour and the individual vortices are no longer examined. Unlike the rectangular wing's tip vortices, which have relatively constant circulation strengths, the flap and tip vortices from the triangular-flapped wing have circulation strengths that decrease rather quickly. However, during this same period, the sum of the flap and tip circulations remains relatively constant. This leads to the conclusion that equal amounts of positive and negative vorticity are cancelling along the interface of these two vortices. Similar trends are observed in other runs that also have relatively large values of $|\overline{\Gamma}_{of}/\overline{\Gamma}_{ot}|$.

The vortex core size, maximum azimuthal velocity, and peak vorticity of the flap and tip vortices versus θ are shown in figure 30 for Run PIV 46. Note that the variables, r_{max}, $u_{\theta max}$ and ω_{max}, have been computed with values of σ that are corrected to remove the artificial increase in the vortex size from aLPT. One interesting observation is the evidence for stretching and tilting of the flap vortex. The flow visualization data at this angle of attack and wing speed reveal that the perturbation on the flap vortex becomes finite by $\theta \approx \pi/2$ radians, causing the flap vortices to stretch and tilt. These three-dimensional effects are strongly evident in all three plots for the flap vortex, which demonstrates a large-amplitude oscillation in r_{max}, $u_{\theta max}$ and ω_{max} at $\theta \approx \pi/2$ radians.

4.3.6. *Enstrophy dispersion*

Since the wakes of the flapped wings contain both positive and negative axial vorticity on each half of the wakes, the use of vorticity in quantifying its dispersion causes difficulties as indicated in § 4.1. Instead, we use the enstrophy distribution $\omega^2(y, z, t)$ to gauge the dispersion of vorticity. Figure 31 shows the behaviour of the total enstrophy EN for Runs 39 and 48 during the development of instabilities as determined using equations (4.3), (4.4) and (4.6). The total enstrophy in figure 31(a) stays nearly constant before the instabilities set in and render the field three-dimensional. It is nearly constant so long as the vortices in a pair mimic two-dimensional vortices ($x/b \sim 35$ in figures 17 and 19). As the instabilities set in, EN drops abruptly, especially for Run 39 for which the effect of the instability is most profound, as seen in figures 4 and 5. Once the instabilities change the flow field from a nearly two-dimensional one into a three-dimensional one, no definitive statements can be made about the behaviour of EN: both for the whole wake and for the two half-wakes of the rectangular wing (Run 11, not shown) It remains nearly constant since the wake is nearly two-dimensional (see figures 3 and 12). The enstrophy dispersion radius r_{EN} defined in equation (4.6) is used as a measure of the dispersion of vorticity in the vortex wakes during the

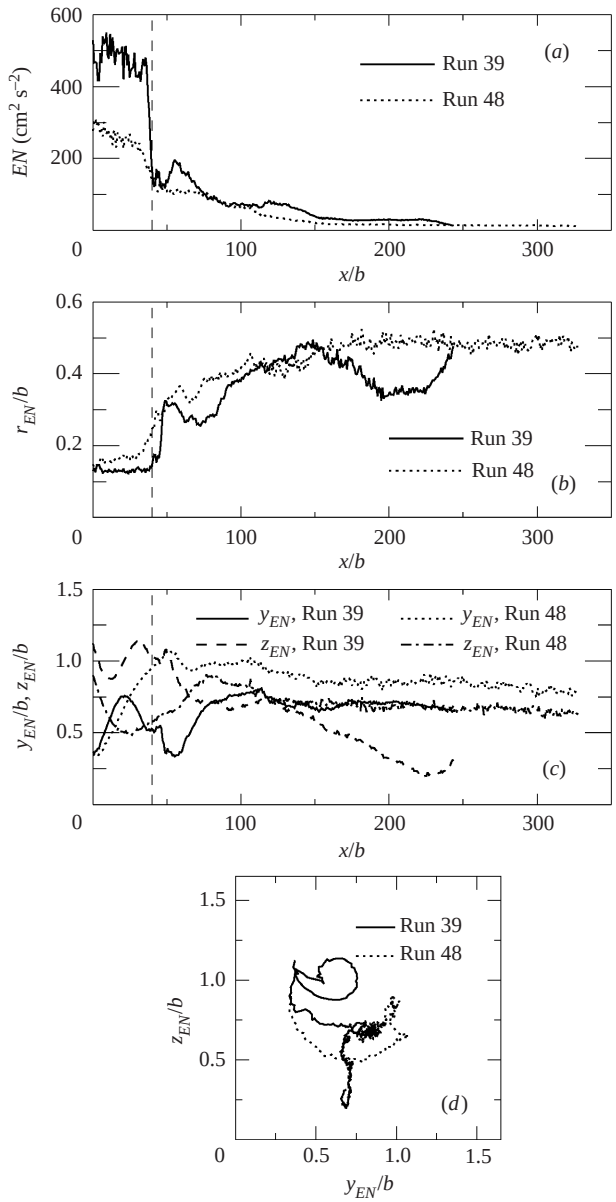

FIGURE 31. The behaviour of total enstrophy EN on one side of the wing during the development of instabilities for Runs PIV 39 and 48: (*a*) total enstrophy, $EN(t)$, (*b*) enstrophy dispersion radius, r_{EN}, (*c*) the centroids $\boldsymbol{y}_{EN}(t)$, and (*d*) trajectories of enstrophy centroids $(y_{EN}(t), z_{EN}(t))$.

development of the instabilities. This quantity has the advantage that it does not rely upon fitting a particular analytical model to the circulation distribution, a feature that proves useful when the wake exhibits highly three-dimensional characteristics. As noted earlier, the use of the vorticity dispersion radius defined in equation (4.5) is inappropriate since opposite-signed vorticity patches are present in the flow. The results for Runs 39 and 48 are shown in figure 31(*b*). As expected, r_{EN} remains constant until the instabilities develop, after which it increases rapidly. The curve for Run 38 shows oscillations which are associated with exchange of substantial amounts of vorticity in

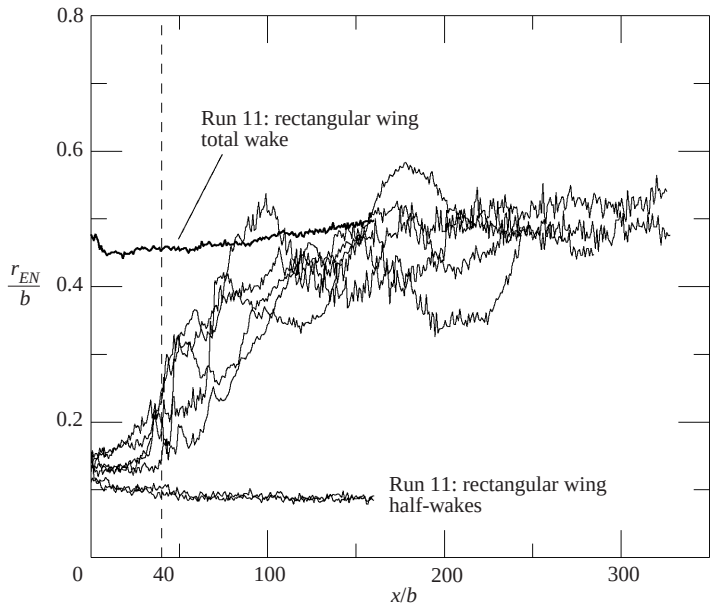

FIGURE 32. Enstrophy dispersion radii r_{EN} during the development of instabilities for Runs PIV 38, 39, 47, 48 and 56 as a function of downstream distance. The vertical dashed line at $x/b = 40$ marks the approximate downstream location where the flap and tip vortices undergo a rapid change in their core structures. The results for the rectangular wing are also shown for reference: the whole wake ($r_{EN} \approx 0.5$) and the two halves ($r_{EN} \approx 0.10$) are shown for Run 11.

the form of rings between the two halves of the wake; r_{EN} reaches a constant value of about $b/2$, suggesting that the vorticity has spread and completely filled the wake of the wing, leaving no more room for further spreading, as corroborated by the flow visualization pictures and vorticity contours. The paths for the enstrophy centroids, (y_{EN}, z_{EN}), are shown in figure 31(c, d). In contrast to the uneventful, almost vertical descent of the wing tip vortices in the wake of the rectangular wing (figure 12), the enstrophy centroids of the flapped wings exhibit seemingly erratic behaviour, following typical cycloids before the instabilities set in. The wake for Run 39 starts to descend and later makes a sharp upwards turn, probably due to vortex patches entering and exiting the data frame. The wake for Run 48, however, seems to hover at a fixed location.

The enstrophy dispersion radius r_{EN} varies strongly as a function of downstream distance. Figure 32 illustrates this for all the sample runs in the figures of this paper ($U_o = 500\,\mathrm{cm\,s^{-1}}$). The vertical dashed line at $x/b = 40$ indicates the approximate downstream distance about which the flap and tip vortices display a sudden change in their structures. Before this change, r_{EN} remains relatively low for all flows, and even constant for some; an expected observation since the initial wake behaviour, hence the spread of vorticity, is determined by the geometric characteristics of the generating wing. The average core sizes of the flap and tip vortices are $0.04b$ and $0.063b$ (table 2) from $0 \leqslant x/b \leqslant 40$. Since the initial vortices are concentrated, r_{EN} is essentially one-half of their separation. Figure 32 indicates a value around $0.14b$. Once the instabilities in the wake undergo severe changes, the total enstrophy as well as its trajectory undergo chaotic changes (see also figure 31). The enstrophy dispersion radius r_{EN} exhibits similar behaviour. In some cases, large oscillations are

Run FV	Run(s) PIV	Re_Γ	$\overline{\Gamma}_{of}/\overline{\Gamma}_{ot}$	b_o^*/b	σ_t/b_o^*	σ_f/b_o^*	d_o/b_o^*	λ_l/b	λ_r/b
1	38–40	103 300	−0.37	1.22	0.050	0.027	0.198	0.9	1.3
2	42–44	60 400	−0.49	1.46	0.039	0.027	0.154	0.9	1.2
3	46–48	52 200	−0.55	1.47	0.038	0.030	0.147	1.1	1.5
4	69	52 400	−0.40	1.63	0.039	0.024	0.144	0.7	0.9
5	70	33 500	−0.57	1.60	0.038	0.028	0.146	1.5	1.3
6	71	23 900	−0.67	1.79	0.035	0.028	0.127	2.3	1.8
7	38–40	103 300	−0.37	1.22	0.050	0.027	0.198	1.1	1.2
8	69	52 400	−0.40	1.63	0.039	0.024	0.144	0.8	0.8
9	42–44	60 400	−0.49	1.46	0.039	0.027	0.154	1.0	1.4
10	70	33 500	−0.57	1.60	0.038	0.028	0.146	1.0	1.0
11	50, 52, 53	103 500	−0.41	1.21	0.051	0.028	0.198	1.0	1.4
12	66	59 100	−0.45	1.37	0.046	0.029	0.152	1.0	1.2
13	55–57	64 700	−0.50	1.37	0.041	0.027	0.161	1.2	1.0
14	64	35 900	−0.57	1.64	0.037	0.027	0.145	1.1	—
15	59–61	46 700	−0.58	1.46	0.040	0.031	0.148	—	1.5
16	—	—	—	—	—	—	—	—	—
17	50, 52, 53	103 500	−0.41	1.21	0.051	0.028	0.198	0.9	1.0
18	66	59 100	−0.45	1.37	0.046	0.029	0.152	1.1	1.0
19	55–57	64 700	−0.50	1.37	0.041	0.027	0.161	1.2	1.3
20	64	35 900	−0.57	1.64	0.037	0.027	0.145	1.0	1.3

TABLE 3. Experimental instability wavelengths. Run FV is the flow visualization run number and Run PIV is the corresponding PIV run number. Re_Γ, average circulated-based Reynolds number from the PIV measurements; $\overline{\Gamma}_{of}/\overline{\Gamma}_{ot}$, average ratio of the flap circulation to the tip circulation from the PIV measurements; b_o^*/b, average, initial distance between the vorticity centroids on either side of the wake; σ_t/b_o^*, average, dimensionless tip vortex size; σ_f/b_o^*, average dimensionless flap vortex size; d_o, average, initial separation distance of the flap and tip vortices; $b = 40$ cm, span of the wing; λ_l/b, average instability wavelength on the left-side flap vortex; λ_r/b, average instability wavelength on the right-side flap vortex.

visible (Run 38, for example). For example, as mentioned in the previous discussion of Run PIV 56 (§4.3.3), a vortex ring from the opposite side of the wake enters the top of the measurement plane at $x/b = 75$, such that a surge in enstrophy is registered. Eventually, however, r_{EN} settles at around $b/2$, apparently a limiting value, since the other half of the vortex wake is undergoing the same processes. The r_{EN} for the two halves as well as the whole wake of the rectangular wing (Run 11) are also shown in the figure. The r_{EN} for the half-wakes remains nearly constant at about $0.1b$ since the wake is essentially two-dimensional. The r_{EN} for the total wake of the rectangular wing is about $0.5b$ since the wake is composed of two concentrated vortices which are nominally a wing span apart (see, for example, figure 12). The slight increase in r_{EN} at later times is consistent with probable wall effects due the bottom of the tank. As the wake approaches the bottom, it slows down and the vortices start moving sideways as seen in figure 12.

The PIV data for the triangular-flapped wings provide a quantitative assessment of the counter-rotating pairs as they evolve in time. From the flow visualization data alone, it was previously difficult to draw firm conclusions about the wakes at large downstream distances because of the dispersal of dye from the vortices. Now, however, questions about the wakes, such as their location, descent properties, kinetic energy, structure, and resulting distribution of vorticity, have been better analysed. In the following section, the instability wavelengths are measured from the flow visualization

data. In Bristol *et al.* (2002*a*), these wavelengths are compared with the results of linear stability analyses and numerical simulations.

5. Observed instability wavelengths

As discussed in § 3, there are two orthogonal views (y, z) of the test section that can be used to take the wavelength measurements from the flow visualization data. Unfortunately, each of these views has a drawback when calculating the unstable wavelengths. Although the side view provides good detail of the instability evolution, it is too close to the test section to measure several wavelengths. The overhead vantage point provides a wide field of view of the test section, but the surface waves from the strut initially distort the appearance of the dye trails. Considering each of these shortcomings, the overhead view is chosen since it typically yields the better measurements of the instability wavelengths. It is necessary, however, to not make measurements while the surfaces waves alter the flow visualization images. In this field of view, the spatial resolution of the flow is 0.26 cm/pixel or $0.007b$/pixel. Another aspect of these wavelength measurements that requires discussion is the manner in which the peaks and troughs are identified. Due to the complexity of the flows, it is difficult to automate the peak and trough location process. Consequently, they are manually measured, which introduces some subjectivity. For the runs at $\alpha = 2.0^\circ$, the peaks and troughs are clearly identifiable. Yet, for the runs at -1.0°, less dye is entrained into the vortices, making it difficult to take wavelength measurements. In these cases, it is sometimes necessary to make an educated guess as to the instability wavelength. The instability wavelengths are measured over several downstream locations from the moment they are first observed until the moment the flap and tip vortices make contact with one another. Because the perturbations are finite in size when the instability is measured, a direct comparison with the results of the linear stability theory in Bristol *et al.* (2002*a*), which assumes that the perturbations are infinitesimal, is difficult. However, it is assumed that the most linearly unstable mode will give rise to finite-size perturbations of the same wavelength, allowing an indirect comparison to be made. On average, the standard deviation of the measured wavelengths is approximately $0.15b$, which is noticeably greater than the spatial resolution of the flow. The reason for this is that the instability wavelengths for each of the counter-rotating vortex pairs vary somewhat over the length of the test section. As the theoretical analyses in Bristol *et al.* (2002*a*) depend critically on the vortex core size, the values of σ were corrected to remove the artificial inflation due to aLPT.

The separation distance, d_o, between the flap and tip vortices is taken from PIV measurements immediately after the wing passes through the light sheet. The PIV measurements are performed on only the right-hand side of the wake, so that the left-hand side pair's separation distance and core sizes are not known. While not exact, it is assumed that the vortices on the left-hand side have the same separation distance and core sizes as those on the right-hand side. Additionally, the distance, b_o^*, between the vorticity centroids in each half of the wake is computed by multiplying the distance from the right-hand centroid to the wing centreline by two.

The experimental instability wavelengths, separation distances, core sizes, and relative circulation strengths are summarized in table 3. Note that the results for a few of the runs are not shown in table 3 because the dye trails are too faint for wavelength measurements to be made. The variables, λ_l/b and λ_r/b, are the average instability wavelengths on the left- and right-hand side flap vortices. It is immediately apparent from table 3 that for the majority of the runs, the observed wavelengths are not equal on either side of the wake. These differences are probably due to small asymmetries

in the wings' construction, leading to variations in the measured wavelengths. For example, consider the top view of Run FV 1, which is shown in figure 6. It can be seen that the indicated left-hand side wavelength is distinctly shorter than that indicated on the right-hand side.

It should be noted that for most of the runs, the average experimental wavelengths are on the order of one span or four times the separation distance of the flap and tip vortices. This observation is consistent with the linear stability analyses in Bristol *et al.* (2002*a*), which show that unequal-strength counter-rotating vortex pairs are most unstable at disturbance wavelengths shorter than that of the classical Crow instability. As the value of Γ increase from -1 to 0, the most unstable wavelength decreases for a particular vortex pair. In Bristol *et al.* (2002*a*), the measured wavelengths in table 3 are shown to agree favourably with those predicted by two- and four-vortex linear stability analyses, demonstrating that the analytical models are capturing the essential physics of the instability. Furthermore, the four-vortex calculations show that the most unstable mode is driven primarily by the instability of the individual vortex pairs. The recent calculations of Fabre, Cossu & Jacquin (2002) have shown remarkable agreement with our observations. In search of optimum perturbations for the growth of instabilities in a four-vortex wakes, they determine the optimum wavelength to be about $\lambda/b \approx 2\pi/7 = 0.9$ for $\Gamma = -0.37$, which is in close agreement with the results in table 3, the variance being within the experimental uncertainty.

6. Closing remarks

Through the vortex wakes of triangular-flapped wings, the stability characteristics and nonlinear evolution of unequal-strength counter-rotating vortex pairs have been studied in a towing tank. These pairs undergo a sinuous instability within 15–20 spans downstream of the triangular-flapped wings. The observed instability wavelengths are typically shorter than that of the classical Crow instability for an equal-strength counter-rotating pair. Furthermore, the flow visualization data illustrate how the nonlinear three-dimensional evolution of the instability varies as the relative strengths of the flap and tip vortices are changed. For smaller values of $|\overline{\Gamma}_{of}/\overline{\Gamma}_{ot}|$, there is a large exchange of vorticity across the wing centreline. However, for larger values of $|\overline{\Gamma}_{of}/\overline{\Gamma}_{ot}|$, the nonlinear vortex interactions remain confined on either side of the wake. The amplification rate of the instability and the orbital rotation rate of a flap-tip vortex pair determine the ejection direction of the vortex rings that form from the evolution of the instability. Using PIV, it is shown that the two-dimensional kinetic energy rapidly drops as the instability becomes finite in amplitude and transforms the two-dimensional nature of the wake into a three-dimensional one. Due to the limited region of the two-dimensional PIV measurements, the total circulation of the counter-rotating pairs is often observed to vary in time as patches of vorticity enter and exit the measurement plane.

The experiments presented here are performed under condition mimicking a quiet unbounded environment. At the beginning of §4, the background velocity field was briefly described. The effect of the finite size of the tank was discussed with reference to figure 12. Also mentioned is the slight side-slippage of the individual vortex trajectories, which may be partly due to large-scale circulation present in the tank and possible asymmetries in wing construction. No attempt was made to systematically explore the effects of the environment on the development of the instabilities discussed here. We do know from observations of airplane wakes in the atmosphere, for example, that the behaviour of the individual vortices as well as interactions among them depend strongly on the state of the background flow field

(Spalart 1996, 1998). Vortex trajectories and strengths strongly depend on background stratification and shear. The background turbulence, both in intensity and scale, has strong influence on the decay of the vortex strength. It seems also very likely that the scale of the background motion will have an effect of the selection of the instability modes. Further, the strength of the background shear will have an influence on the amplification rate of the instabilities. However, each of these effects is complicated enough to warrant separate research, and hence has not been addressed systematically during the course of the experiments described here.

The initial linear instability and the eventual nonlinear dynamics of the vortex filament are observed to be stationary in the laboratory coordinate system. No preferential motion either toward or away from the moving wing is noticeable. When the events are observed from the reference frame of the wing, the originator of the disturbances, they look as if they are being convected away from the wing with the towing speed. In this reference frame and within the convention of stability analysis, the instability is said to be *convective* (Drazin & Reid 1981; Huerre & Monkewitz 1990; Fabre *et al*. 2000). There is still the possibility that these instabilities are excited by the background broadband disturbances, in which case one might argue that the instabilities are *absolute* since they are stationary in that reference frame. This possibility is rather remote since several of the experimental runs are made after the tank has been left undisturbed for several days. This distinction, however, is not essential for the discussion in this paper.

In a companion paper, Bristol *et al.* (2002*a*) discuss the physical mechanisms that cause the instability between unequal-strength counter-rotating vortex pairs. Additionally, a comparison of the observed wavelengths in § 5 will be made with the results of linear stability analyses and numerical simulations. Finally, from a practical standpoint, the wake alleviation properties of this instability are assessed in Ortega *et al.* (2002) by comparing the rolling moment and downwash in the wakes of the rectangular and triangular-flapped wings.

R. L. Bristol and J. M. Ortega were recipients of National Science Foundation Graduate Fellowships.

REFERENCES

Batchelor, G. K. 1967 *An Introduction to Fluid Dynamics*. Cambridge University Press.

Bilanin, A. J., Teske, M. E. & Williamson, G. G. 1977 Vortex interactions and decay in aircraft wakes. *AIAA J*. **15**, 250–260.

Bristol, R. L. 2000 Co-operative wake vortex instabilities. PhD Dissertation, University of California, Berkeley.

Bristol, R. L., Ortega, J. M., Marcus, P. S. & Savaş, Ö. 2002*a* Co-operative wake vortex instabilities. In preparation.

Bristol, R. L., Ortega, J. M. & Savaş, Ö. 2002*b* Experimental study of corotating wake-vortex merger at Reynolds numbers of order 10^5. *AIAA J*. (submitted).

Chen, A., Jacob, J. & Savaş, Ö. 1999 Dynamics of corotating vortex pairs in the wakes of flapped airfoils. *J. Fluid Mech.* **383**, 155–193.

Corsiglia, V. R. & Dunham, R. E. 1976 Aircraft wake vortex minimization by use of flaps. *NASA Symp. on Wake Vortex Minimization*, *NASA SP-409*, pp. 305–338.

Crouch, J. D. 1997 Instability and transient growth for two trailing-vortex pairs. *J. Fluid Mech.* **350**, 311–330.

Crow, S. C. 1970 Stability theory for a pair of trailing vortices. *AIAA J*. **8**, 2172–2179.

Drazin, P. G. & Reid, W. H. 1981 *Hydrodynamic Stability*. Cambridge University Press.

Fabre, D., Cossu, C. & Jacquin, L. 2000 Spatio-temporal development of the long and short-wave vortex-pair instabilities. *Phys. Fluids* **12**, 1247–1250.

Fabre, D. & Jacquin, L. 2000 Stability of a four-vortex aircraft wake model. *Phys. Fluids* **12**, 2438–2443.

Fabre, D., Jacquin, L. & Loof, A. 2002 Optimal perturbations in a four-vortex aircraft wake in counter-rotating configuration. *J. Fluid Mech.* **451**, 319–328.

Huerre, P. & Monkewitz, P. A. 1990 Local and global instabilities in spatially developing flows. *Annu. Rev. Fluid Mech.* **22**, 473–537.

Kida, S. & Takaoka, M. 1994 Vortex reconnection. *Annu. Rev. Fluid Mech.* **26**, 169–189.

Klein, R. & Majda, A. J. 1993 An asymptotic theory for the nonlinear instability of antiparallel pairs of vortex filaments. *Phys. Fluids* **5**, 369–379.

Klein, R., Majda, A. J. & Damodaran, K. 1995 Simplified equations for the interaction of nearly parallel vortex filaments. *J. Fluid Mech.* **288**, 201–248.

Lamb, H. 1938 *Hydrodynamics*. Dover.

Leonard, A. 1974 Numerical simulation of interacting, three-dimensional vortex filaments. *Proc. 4th Int Conf. on Numerical Methods in Fluid Dynamic, Boulder Colorado, June 24–28*, pp. 245–250, 1974; also Lecture Notes in Physics, vol. 35, Springer, 1975.

Leweke, T. & Williamson, C. H. K. 1998 Cooperative elliptic instability of a vortex pair. *J. Fluid Mech.* **360**, 85–119.

Marcus, P. S. 1990 Vortex dynamics in a shearing zonal flow. *J. Fluid Mech.* **215**, 393–430.

Melander, M. V. & Hussain F. 1989 Cross-linking of two antiparallel vortex tubes. *Phys. Fluids* A **1**, 633–636.

Ortega, J. M. 2001 Stability characteristics of counter-rotating vortex pairs in the wakes of triangular-flapped airfoils. PhD Dissertation, University of California, Berkeley.

Ortega, J. M., Bristol, R. L. & Savaş, Ö. 2002 Wake alleviation properties of triangular-flapped wings. *AIAA J.* **40**(4), 709–721.

Ortega, J. M. & Savaş, Ö. 2001 A rapidly growing instability mode in trailing multiple-vortex wakes. *AIAA J.* **39**, 750–754.

Quackenbush, T. R., Batcho, P. F., Bilanin, A. J. & Carpenter, B. F. 1998 Design, fabrication, and test planning for an SMA-actuated vortex wake control system. Smart Structures and Materials 1998, Industrial and Commercial Applications of Smart Structure Technologies, 3–5, March 1998. *Proc. SPIE* **3326**, 259–271.

Quackenbush, T. R., Bilanin, A. J., Batcho, P. F., McKillip, R. M. Jr. & Carpenter, B. F. 1997 Implementation of vortex wake control using SMA-actuated devices. Smart Structures and Materials 1997, Industrial and Commercial Applications of Smart Structure Technologies, 4–6, March 1997. *Proc. SPIE* **3044**, 134–146.

Quackenbush, T. R., Bilanin, A. J. & Carpenter, B. F. 1999 Test results for an SMA-actuated vortex wake control system. Smart Structures and Materials 1999, Industrial and Commercial Applications of Smart Structure Technologies, March 1999. *Proc. SPIE* **3674**, 84–94.

Quackenbush, T. R., Bilanin, A. J. & McKillip, R. M. Jr 1996 Vortex wake control via smart structures technology. In *Smart Structures and Materials 1996, Industrial and Commercial Applications of Smart Structure Technologies, 27–29, February 1996. Proc. SPIE* **2721**, 78–92.

Rennich, S. C. & Lele, S. K. 1999 A method for accelerating the destruction of aircraft wake vortices. *J. Aircraft* **36** 398–404.

Rossow, V. J. 1999 Lift-generated vortex wakes of subsonic transport aircraft. *Progress in Aerospace Sciences* **35**(6), 507–660.

Saffman, P. G. 1990 A model of vortex reconnection. *J. Fluid Mech.* **212**, 395–402.

Saffman, P. G. 1992 *Vortex Dynamics*. Cambridge University Press.

Scorer, R. S. & Davenport, L. J. 1970 Contrails and aircraft downwash. *J. Fluid Mech.* **43**, 451–464.

Shelley, M. J., Merion, D. I. & Orszag, S. A. 1993 Dynamical aspects of vortex reconnection of perturbed anti-parallel vortex tubes. *J. Fluid Mech.* **246**, 613–652.

Sholl, M. J. & Savaş, Ö. 1998 A fast Lagrangian PIV method for study of general high-gradient flows. *AIAA Paper* 97-0493.

Spalart, P. R. 1996 On the motion of laminar wing wakes in a stratified fluid. *J. Fluid Mech.* **327**, 139–160.

Spalart, P. R. 1998 Airplane trailing vortices. *Annu. Rev. Fluid Mech.* **30**, 107–138.

Tsuei, L. & Savaş, Ö. 2000 Treatment of interfaces in particle imaging velocimetry. *Exps. Fluids* **29**, 203–214.

Widnall, S. E., Bliss, D. B. & Tsai, C.-Y. 1974 The instability of short waves on a vortex ring. *J. Fluid Mech.* **66**, 35–47.